nature cell biology

Article

https://doi.org/10.1038/s41556-026-01877-0

Adaptor-mediated recruitment of three dyneins to dynactin enhances force generation

Received: 26 March 2025

Accepted: 12 January 2026

Published online: 16 February 2026

Check for updates

Lu Rao[1] ✉, Xinglei Liu[1], Mirjam Arnold[2], Kyoko Okada[3], Richard J. McKenney[3], Kristy Stengel[2], Simone Sidoli[4], Florian Berger[5] & Arne Gennerich[1] ✉

Cytoplasmic dynein is an essential microtubule motor protein that powers organelle transport and mitotic spindle assembly. Its activity depends on dynein–dynactin–cargo adaptor complexes, such as dynein–dynactin–BicD2, which typically function with two dynein motors. We show that mechanical tension recruits a third dynein motor via an auxiliary BicD2 adaptor binding the light intermediate chain of the third dynein, stabilizing multidynein assemblies and enhancing force generation. Lis1 prevents dynein from transitioning into a force-limiting phi-like conformation, allowing single-dynein dynein–dynactin–BicD2 to sustain forces up to approximately 4.5 pN, whereas force generation often ends at about 2.5 pN without Lis1. Complexes with two or three dyneins generate 7 pN and 9 pN, respectively, consistent with a staggered motor arrangement that enhances collective output. Under load, dynein–dynactin–BicD2 primarily takes 8-nm steps, challenging existing dynein coordination models. These findings reveal adaptive mechanisms that enable robust intracellular transport under varying mechanical demands.

Cytoplasmic dynein-1 is the primary microtubule minus-end-directed motor in eukaryotic cells, where it drives essential processes ranging from organelle transport and mitotic spindle positioning to neuronal development[1–6]. To carry out these diverse tasks, dynein must produce sustained forces and move processively along microtubules, properties that are tightly controlled by cofactors. Among these, lissencephaly-1 (Lis1) is of particular importance: it is essential for brain development[7–13], and loss of Lis1 function results in severe Type I lissencephaly[14–18]. Although Lis1 clearly modulates dynein's ability to generate motion and force[19], the precise mechanistic basis of this regulation remains incompletely understood.

Dynein function is further regulated by its interaction with dynactin, a large multi-subunit complex that enhances dynein's processivity[1,3,20–30], increases its on-rate[22,23] and tethers it to specific cellular cargoes[5,31,32]. Mutations in dynactin subunits cause neurodegenerative diseases[33–35], underscoring its physiological importance. Furthermore, a coiled-coil cargo adaptor such as Bicaudal-D2 (BicD2) bridges the dynein tail and the dynactin shoulder[36,37] (Fig. 1a), converting autoinhibited dynein—which is diffusive[38] or weakly processive[39,40]—into a highly processive motor[22,23,41]. Structural work has revealed that cargo adaptors like BicD2 can recruit two dyneins to dynactin (D_2DB), forming dynein–dynactin–adaptor (DDA) assemblies with four aligned motor domains[42,43] (Fig. 1a). Structural studies of dynein–dynactin–BICDR1 (DDR) complexes have identified a second auxiliary BICDR1 adaptor bound to dynactin[44], although its functional role remains unknown. In BicD2- and BICDR1-mediated assemblies, the two-dynein

[1]Department of Biochemistry and Gruss Lipper Biophotonics Center, Albert Einstein College of Medicine, Bronx, NY, USA. [2]Department of Cell Biology, Albert Einstein College of Medicine, Bronx, NY, USA. [3]Department of Molecular and Cellular Biology, University of California Davis, Davis, CA, USA. [4]Department of Biochemistry, Albert Einstein College of Medicine, Bronx, NY, USA. [5]Cell Biology, Neurobiology and Biophysics, Department of Biology, Faculty of Science, Utrecht University, Utrecht, The Netherlands. ✉e-mail: lu.rao@einsteinmed.edu; arne.gennerich@einsteinmed.edu

configuration enhances force output through load sharing and reduces microtubule detachment, thereby increasing processivity[43].

Lis1 also acts within these assemblies but its function has been difficult to reconcile among studies. Early biochemical work suggested that Lis1 inhibits dynein by uncoupling its ATPase cycle from microtubule binding[45–47]. More recent studies, however, indicate that Lis1 instead activates dynein by preventing the autoinhibited 'phi' conformation[48–56] (named for its resemblance of the Greek letter Φ) and by promoting the formation of DDA complexes with two dyneins[19,57]. Because Lis1 dissociates following microtubule engagement[58], its primary role may lie in switching dynein from an inactive to an active assembly state rather than in modulating motility directly. Although these findings advanced our understanding of how Lis1 primes dynein for motility, it remains unclear how Lis1 contributes to force generation within fully assembled DDA complexes.

Despite substantial progress in understanding DDA organization and function, several fundamental questions remain. First, how does the force generated by a DDA complex depend on the number of dyneins it contains? Two-dynein assemblies exist but whether this represents the maximal functional configuration—or whether additional dyneins can be recruited under physiological conditions—remains unclear. Second, how do DDA complexes adapt to mechanical load? Dynein operates in a viscous and crowded cytoplasm, and increasing load could alter the engagement, activation state or number of motors in ways not captured in static structural studies. Third, how Lis1 influences these load-dependent behaviours remains unclear. Although Lis1 prevents the autoinhibited dynein state and promotes the formation of two-dynein complexes, whether Lis1 also modulates how DDA complexes respond to increasing mechanical resistance is not known. Resolving these questions is essential for understanding how dynein achieves robust transport under the complex and dynamic mechanical demands of the intracellular environment.

Here we combine optical trapping, multicolour single-molecule fluorescence and structural analyses to interrogate how dynein–dynactin–BicD2 (DDB) complexes behave under load and how Lis1 contributes to their activation. Our results reveal three interconnected principles of dynein regulation. First, dynein force generation is limited by a phi-like autoinhibited conformation[19,57,59] that restricts single-dynein DDB complexes (D_1DB) to forces of approximately 2.5 pN; relieving this autoinhibition—either through Lis1 or mutation—enables D_1DB to generate forces of up to 4.5 pN. Second, DDB complexes adapt to increasing load by recruiting a third dynein (D_3DB) via an auxiliary BicD2 adaptor that binds the light intermediate chain (LIC) of the additional motor, forming a higher-order assembly that increases force output. Two-dynein and three-dynein complexes stall at loads of approximately 7 and 9 pN, respectively, suggesting a staggered motor arrangement with uneven load distribution. Third, fully assembled DDB complexes display predominantly 8-nm centre-of-mass steps under load, consistent with a compact motor arrangement, whereas the engagement of the third dynein reduces step size to about 4 nm near stall. Together, these findings define a load-dependent regulatory mechanism that integrates Lis1-mediated activation, adaptor-mediated recruitment of a third dynein and multidynein coordination, providing a conceptual framework for how dynein complexes meet the mechanical challenges of intracellular transport.

Results

'Trains' of DDB force generation reveal distinct stalling forces

Previous studies on DDB force generation have primarily utilized non-native axonemes—160-nm thick microtubule-containing structures purified from sea urchin[60]—and substoichiometric DDB concentrations (dynein:dynactin:BicD2 molar ratios of 1:5:2, ref. 61; 1:5:20, refs. 43,62; and 1:2:10, ref. 19). These conditions disfavoured the formation of DDB complexes with two dyneins and limited the detection of distinct force-generation states.

For example, when DDB is tethered to trapping beads via a motorless dynein tail, which permits only one dynein to bind while the second dynein-binding site is occupied by the tail fragment, the complex generates a force of 3.7 ± 0.2 pN (mean ± s.e.m.) on axonemes[19]. This force matches that generated by DDB linked to beads via BicD2 (ref. 43), suggesting that these studies primarily involved complexes with only a single dynein. Similarly, *Saccharomyces cerevisiae* dynein alone generates 3.6 ± 0.2 pN on axonemes[61] and 4.50 ± 0.04 pN on microtubules[40,63], indicating potential differences in DDB behaviour on microtubules.

To investigate the function of DDA complexes with two dynein motors (D_2DA; Fig. 1a), previous studies assembled motor complexes using the cargo adaptors HOOK3 and BICDR1, which are more likely than BicD2 to recruit two dyneins to dynactin[43]. As dynein–dynactin–HOOK3 (4.9 ± 0.2 pN)[43] and DDR (6.5 ± 0.3 pN)[43] generate more force than DDB (3.7 ± 0.2 pN)[43], it was reasoned that dynein–dynactin–HOOK3 and DDR recruit two dyneins. However, these studies were conducted on axonemes, which are commonly co-purified with other axoneme-associated proteins[64,65]. They also used a 1:5 molar dynein–dynactin ratio[43,62], conditions under which, on average, only one in five dynactin complexes can bind a dynein. Thus, these complexes were unlikely to be fully saturated with two dyneins, leaving the source of their higher force generation unclear.

To address these limitations and gain insights into force production, we conducted optical-trapping experiments using DDB complexes purified from rat-brain lysate with an amino-terminal domain of the dynein-activating adaptor BicD2 (BicD2–superfolder green fluorescent protein (sfGFP), amino acids 25–400)[22]. As neither dynein nor dynactin alone bind to BicD2 (ref. 22), we anticipated that these complexes would contain dynein and dynactin in a 1:1 or 2:1 ratio. We then employed 500-nm trapping beads covalently linked to anti-GFP and used microtubules instead of axonemes. Strikingly, we observed extended trains of force-generation events characterized by rapid force increases, followed by stalling of movement (Fig. 1b). These force trains revealed four distinct stall forces for DDB: approximately 2.5, 4.5, 7.0 and 9.0 pN (Fig. 1b,c). This discovery contrasts with earlier studies that reported broad detachment forces encompassing the plateaus we identified in our analyses (2–7 pN for DDB, 2.5–9.0 pN for dynein–dynactin–HOOK3 and 3–11 pN for DDR)[51,55]. We speculate that the detection of these distinct plateaus in our experiments is due to the use of smaller beads, which, due to lower vertical forces, are likely to increase the DDB-microtubule on-rate and the likelihood of observing stalling (note that the effects of varying vertical forces on human dynein have not been tested but higher vertical forces enhance microtubule detachment of kinesin-1 and prevent motor stalling[66,67]).

D_1DB stalls at 2.5 or 4.5 pN depending on its partial or full activation

Because DDB complexes purified from rat-brain lysate contained a heterogenous mixture of one-dynein and two-dynein assemblies (Extended Data Fig. 1a) that generated a broad range of forces (Fig. 1b–d), we sought to control the stoichiometry of the components to better resolve each force profile. In addition, because we typically observed only 1–2 events per bead at forces of approximately 9 pN (Fig. 1d), we reasoned that the interaction between anti-GFP and sfGFP might not be strong enough to sustain large forces over time. To overcome this limitation, we used streptavidin-coated beads instead of anti-GFP-coated beads, taking advantage of the robust streptavidin–biotin linkage, which withstands forces up to 60 pN in force-extension experiments[68].

We purified recombinant full-length human dynein co-expressed with its five accessory chains, as previously described[23] (Extended Data Fig. 1b(left)). Biotinylated BicD2 (amino acids 25–400) was expressed in *Escherichia coli* and purified (Extended Data Fig. 1b(right)). Dynactin was purified from a human suspension culture cell line by tagging the DCTN4 subunit following established protocols[69,70]

https://doi.org/10.1038/s41556-026-01877-0

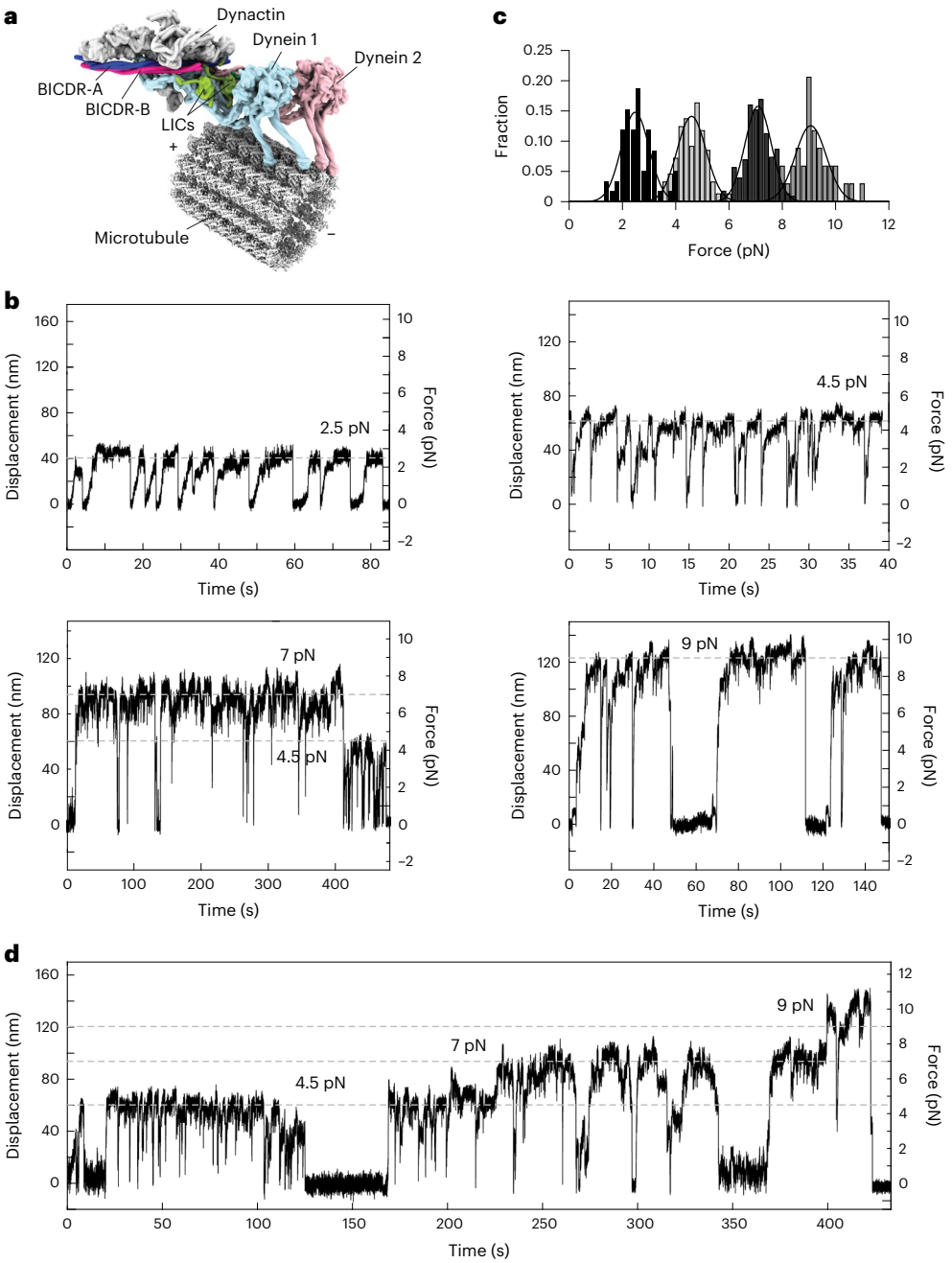

Fig. 1 | Structure of the microtubule-bound DDR complex and DDB force generation. a, Structural representation of the DDR complex (Protein Data Bank (PDB), 7Z8F)[72]. The dynein heavy chain from the DDR complex was aligned with microtubules (PDB, 6DPV; Electron Microscopy Data Bank, 7974)[100] using the high-affinity dynein microtubule-binding domain structure bound to microtubules (PDB, 6KIQ)[101]. **b**, Representative traces of DDB-mediated force generation. Traces have been downsampled by a factor of 400 for visualization. **c**, DDB complexes bound to anti-GFP-coated beads exhibit stalling at four force levels (2.48 ± 0.04 pN, $n = 59$; 4.60 ± 0.02 pN, $n = 153$; 7.10 ± 0.02 pN, $n = 231$; and 9.10 ± 0.05 pN, $n = 34$; mean ± s.e.m. from Gaussian fits) following a bead-wash step. **d**, Representative trace of DDB-mediated force generation showing stepwise increases in force. Traces were downsampled by a factor of 400 for visualization.

(Extended Data Fig. 1b(middle)) instead of using traditional sources such as bovine, porcine or rodent brain tissue[20,22,23]. With each component—dynein, BicD2 and dynactin (expressed and purified to high purity)—we successfully assembled DDB complexes in defined stoichiometric ratios.

To investigate the force generation of DDB when associated with a single dynein, we assembled the complexes in a 1:1:1 ratio of dynein, dynactin and BicD2. Our previous studies have indicated that isolated human dynein can transition from slow movement towards 2.5 pN to a rapid movement towards 4 pN (Fig. 2a). We observed similar behaviour in DDB complexes, transitioning from slow movement towards 2.5 pN, followed by rapid movement towards 4.5 pN (Fig. 2b).

Interestingly, for human dynein in isolation, we only observed instances of transitioning from 2.5 to 4.0 pN under increased trap stiffnesses (approximately 0.06 pN nm^{-1})[40]; at a lower trap stiffness of 0.01 pN nm^{-1}, it stalls at around 1 pN (Fig. 2a(inset)), suggesting that a higher force per unit displacement facilitates the full activation of dynein. This observation indicates that the two distinct forces are generated by a single dynein altering its behaviour depending on its activation state.

https://doi.org/10.1038/s41556-026-01877-0

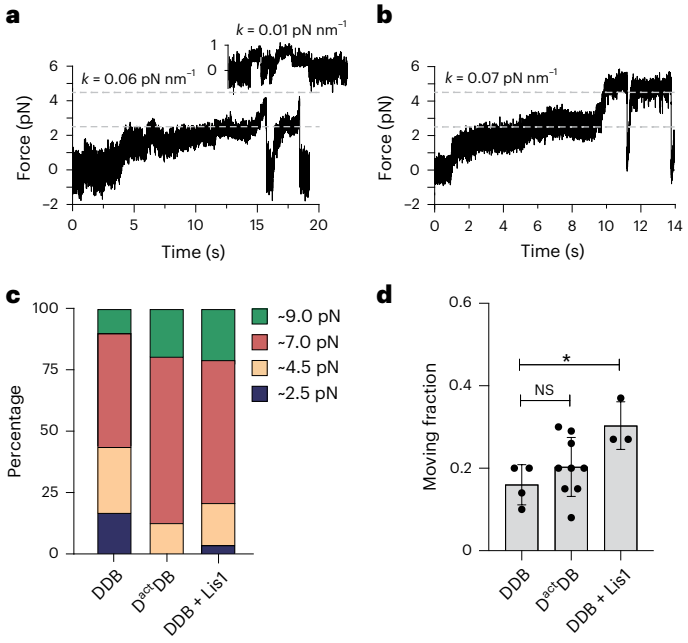

Fig. 2 | A phi-like autoinhibitory conformation underlies stalling at 2.5 pN. **a**, Force generation of human dynein measured in a stiff optical trap, where k denotes the trap stiffness (k = 0.06 pN nm^{-1}). The inset shows reduced force generation in a weak trap (k = 0.01 pN nm^{-1}), where dynein processivity becomes limiting. **b**, D_1DB force trace showing a transition from slow movement towards approximately 2.5 pN to rapid movement towards 5 pN. **c**, Stall-force distributions for DDB, D^{act}DB and DDB + Lis1. Fractions of beads generating 2.5, 4.5, 7.0 and 9.0 pN: DDB, 17, 27, 46 and 10%, respectively (n = 41 total moving beads); D^{act}DB, 0, 13, 68 and 19%, respectively (n = 31); DDB + Lis1, 3, 17, 59 and 21%, respectively (n = 29). One-sided two-proportion Z-test: DDB versus D^{act}DB, P = 0.016 (2.5 pN), 0.150 (4.5 pN), 0.07 (7 pN) and 0.244 (9 pN); DDB versus DDB + Lis1, P = 0.078 (2.5 pN), 0.347 (4.5 pN), 0.311 (7 pN) and 0.198 (9 pN). **d**, Fraction of force-generating beads per experiment (mean ± s.d.): DDB, 0.16 ± 0.05 (n = 4 experimental replicates), D^{act}DB, 0.20 ± 0.07 (n = 9) and DDB + Lis1, 0.30 ± 0.06 (n = 3). Two-sided unpaired Kolmogorov–Smirnov test; NS, not significant (P = 0.48), *P = 0.029. Panel **a** adapted with permission from ref. 40, AAAS.

Recent studies have shown that mammalian dynein often adopts an autoinhibited conformation, commonly referred to as the phi particle[50–53,55], which hinders efficient interactions with microtubules. Unlike mammalian dynein, *S. cerevisiae* dynein moves processively along microtubules by itself[71] and a mutant form that is unable to assume the phi conformation exhibits an increased run length along microtubules[48], indicating that the autoinhibited state limits the movement of wild-type *S. cerevisiae* dynein on microtubules. To investigate whether a similar autoinhibited state restricts human dynein's force generation to approximately 2.5 pN, we assembled DDB complexes at a 1:1:1 ratio with a dynein mutant (K1610E and R1567E double mutant)[50] that cannot adopt this inhibitory conformation. We refer to these complexes as D^{act}DB, denoting an 'activated' dynein. Contrary to expectations, D^{act}DB complexes predominantly stalled at around 7 pN (Fig. 2c and Extended Data Fig. 2a; trend towards increased 7 pN fraction compared with DDB, P = 0.07). This behaviour persisted even when complexes were assembled at a 1:6:6 molar ratio or in the presence of excess dynein tail (amino acids 1–1455; ref. 43; Extended Data Figs. 1c and 2b; not significant, P = 0.78 and 0.95 versus D^{act}DB, respectively), suggesting that dynein in its open conformation preferentially forms DDB complexes with two dyneins per complex (discussed further in the next section).

However, as hypothesized, this dynein mutant prevents stalling at approximately 2.5 pN in the lower force regime, with only forces of 4.5 pN observed (Fig. 2c and Extended Data Fig. 2a,b). Moreover, the inclusion of Lis1, which prevents dynein's autoinhibited state[19,48,49,54,57], showed a trend towards reducing the occurrence of stalling at 2.5 pN (Fig. 2c; P = 0.078 versus DDB) and significantly increased the fraction of active DDB complexes (Fig. 2d; P = 0.029 versus DDB). These results confirm that a DDB complex bound to a single dynein stalls at either 2.5 or 4.5 pN, depending on whether it can transition into phi-like conformation or not.

Fully active D_2DB stalls at 7 pN

D^{act}DB complexes generate forces of approximately 4.5, 7 or 9 pN (Extended Data Fig. 2a), suggesting that fully active D_1DB generates 4.5 pN, whereas D_2DB, a complex with two dyneins, generates 7 pN. This aligns with observations of DDR, which preferentially binds two dyneins and has been reported to generate 6.5 pN (ref. 43).

A key question is what accounts for the observed stalling at 9 pN (Fig. 1b–d). If fully active D_1DB generates 4.5 pN, then logically, fully active D_2DB might be expected to reach up to 9 pN if both motors contribute equally to force generation. However, DDR assembled with the dynein mutant and in the presence of Lis1—both intended to prevent the phi conformation—has been observed to generate only 6.1 pN (ref. 19), which aligns more closely with the force of 7 pN we observe. This discrepancy suggests that the 7-pN stall force does not arise from a collaboration between a fully active dynein and a partially active motor. It instead probably results from uneven load distribution between the motors, with the leading motor bearing a greater load than the lagging dynein, contributing only about 2.5 pN.

To provide further support for the hypothesis that the 7-pN force is generated by two actively engaged dyneins, we introduced excess dynein (5 nM) into a slide chamber containing DDB complexes pre-assembled at 1:1:1 ratios bound to trapping beads. Under these conditions, approximately 60% of the moving beads displayed forces of 7 pN (Fig. 3a and Extended Data Fig. 2c). Importantly, the overall fraction of beads generating force remained comparable to that of DDB-only complexes (approximately 10%), even after the addition of excess dynein (Fig. 3b). This suggests that freely diffusing dyneins selectively bind to DDB complexes anchored via the biotinylated BicD2 to the bead surfaces, rather than binding non-specifically to the bead surfaces, which would have increased the fraction of force-generating beads[40]. By contrast, the addition of excess dynein tail (5 nM) lacking the motor domain reduced the percentage of 7-pN forces (trend towards reduction versus DDB, P = 0.074), consistent with displacement of a full dynein from DDB[62] (Fig. 3a).

Auxiliary BicD2 enables recruitment of a third dynein to DDB and enhanced force generation

Given the observed force trains at about 9 pN and the probable contribution of two fully active dyneins to the 7-pN force, we hypothesized that the 9-pN force results from the functional recruitment of a third dynein to the DDB complex. Supporting this idea, both the addition of excess dynein tail (Fig. 3a) and the removal of excess dynein from pre-assembled DDB complexes via bead centrifugation prevented 9-pN forces (Extended Data Fig. 2d). Although the possibility that a third dynein binds has not been previously discussed, the structure of two dyneins bound to dynactin and BICDR1 (determined using cryogenic electron microscopy, cryo-EM)[43] suggests that the dynactin shoulder provides sufficient space for a third dynein tail to bind (Fig. 3c,d). Moreover, the vacant segment of BicD2 contains two acidic patches resembling the four acidic sites that mediate binding of the first and second dynein tails (Fig. 3c(bottom)).

To test this hypothesis, we examined whether dynactin can accommodate a third dynein by generating two truncated BicD2 constructs, BicD2(25–276) and BicD2(25–180), based on the cryo-EM structure of DDB[43] (Fig. 3e). BicD2(25–276) spans the full shoulder of dynactin, encompassing the putative third dynein-binding site (Fig. 3c,f),

https://doi.org/10.1038/s41556-026-01877-0

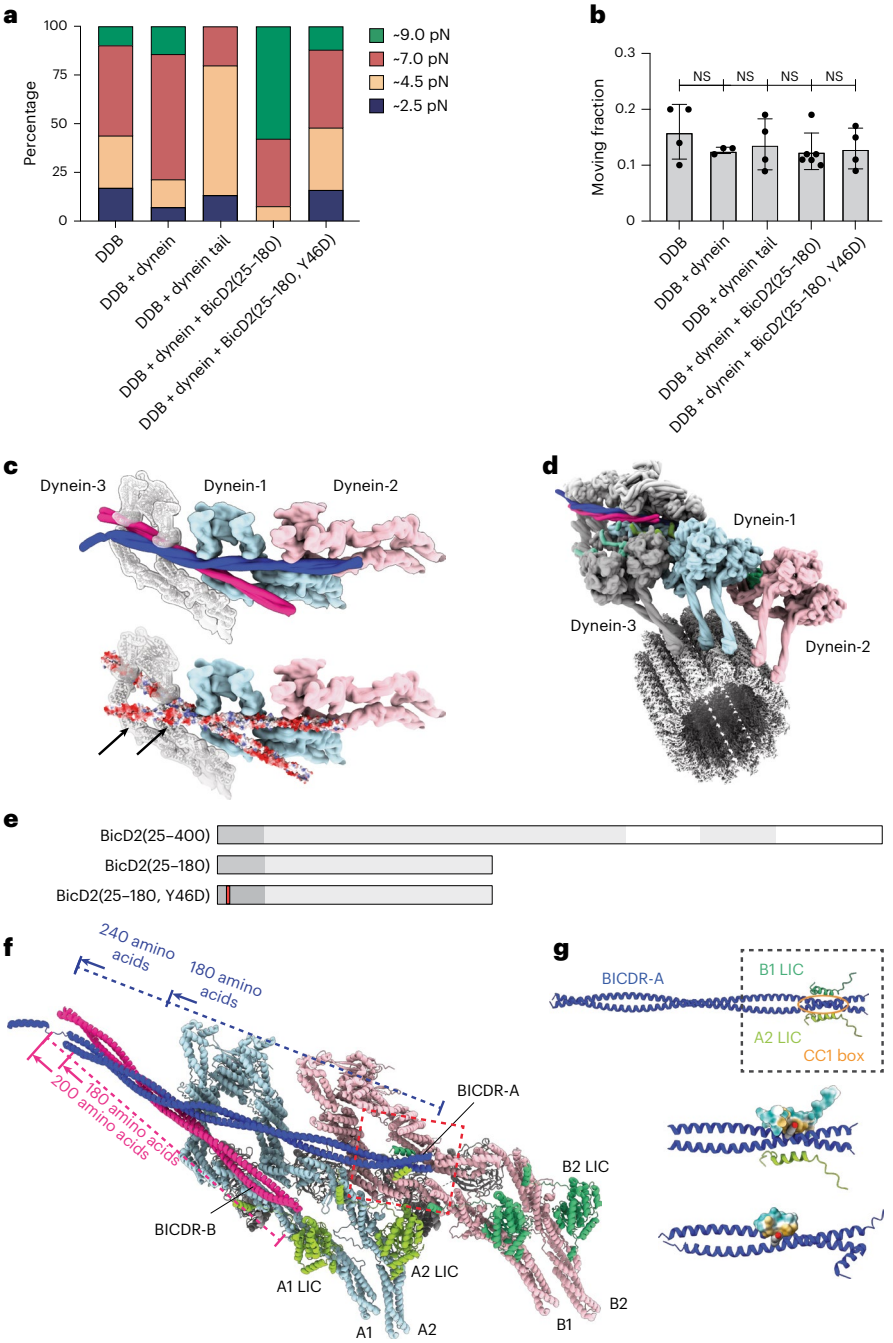

Fig. 3 | DDB activity states and predicted third-dynein recruitment. a, Stall-force distributions for DDB complexes incubated with excess dynein. Fractions of beads generating 2.5, 4.5, 7 and 9 pN: DDB, 17, 27, 46 and 10%, respectively ($n = 41$); DDB + dynein, 7, 14, 64 and 15%, respectively ($n = 14$); DDB + dynein tail, 13, 67, 20 and 0%, respectively ($n = 15$); DDB + dynein + BicD2(25–180), 0, 8, 35 and 57%, respectively ($n = 26$); and DDB + dynein + BicD2(25–180, Y46D), 16, 32, 40 and 12%, respectively ($n = 25$). One-sided two-proportion Z-test: DDB versus DDB + dynein, $P = 0.363$, $P = 0.340$, $P = 0.246$ and $P < 0.639$; DDB versus DDB + dynein tail, $P = 0.736$, $P = 0.006$, $P = 0.074$ and $P = 0.209$; DDB versus DDB + dynein + BicD2(25–180), $P = 0.026$, $P < 0.054$, $P < 0.343$ and $P < 0.001$; DDB versus DDB + dynein + BicD2(25–180, Y46D), $P = 0.909$, $P = 0.653$, $P < 0.615$ and $P < 0.774$; DDB + dynein versus DDB + dynein + BicD2(25–180), $P = 0.168$, $P = 0.507$, $P = 0.072$ and $P = 0.008$; DDB + dynein + BicD2(25–180) versus DDB + dynein + BicD2(25–180, Y46D), $P = 0.034$, $P = 0.029$, $P = 0.691$ and $P < 0.001$ for 2.5, 4.5, 7.0 and 9.0 pN, respectively. **b**, Fraction of force-generating beads. DDB, 0.16 ± 0.05 (mean ± s.d.; $n = 4$ experimental replicates); DDB + dynein (0.13 ± 0.01, $n = 3$); DDB + dynein tail (0.14 ± 0.05, $n = 4$); DDB + dynein + BicD2(25–180) (0.12 ± 0.03, $n = 6$); and DDB + dynein + BicD2(25–180, Y46D) (0.13 ± 0.04, $n = 4$). One-way analysis of variance with Dunnett's test; $P = 0.73$, 0.89, 0.55 and 0.74, respectively, versus DDB; NS, not significant. **c**, Predicted binding site for a third dynein (grey) added to DDR structure (PDB, 7Z8F; top). AlphaFold3 model of BicD2(18–240) (electrostatic surface; red, negative) overlaid with BICDR1 from DDR highlights two additional acidic patches (arrows) potentially engaging the third dynein (bottom); BicDR hidden for clarity. **d**, Full DDR complex with added dynein (grey) and microtubule. **e**, BicD2 constructs used. The Y46D mutation in BicD2(25–180) is shown in red. **f**, DDR structure with two dyneins (light blue and pink) and two BICDR1 dimers (blue and magenta; PDB, 7Z8F); dynactin was omitted. The interaction between the C-terminal LIC helices of dynein A2 (light green) and B1 (green) and the N-terminal CC1 box of BICDR-A (blue) is highlighted (dashed red box). **g**, ColabFold[102] model of mouse BicD2(25–180) bound to human dynein LIC(417–444) (top), with a magnified view showing Tyr46 (spheres) and LIC hydrophobic surface (yellow, hydrophobic; cyan, hydrophilic; middle). The human BicD2(1–98)–LIC(433–458) crystal structure is shown for comparison (PDB, 6PSE; ref. 73; bottom).

https://doi.org/10.1038/s41556-026-01877-0

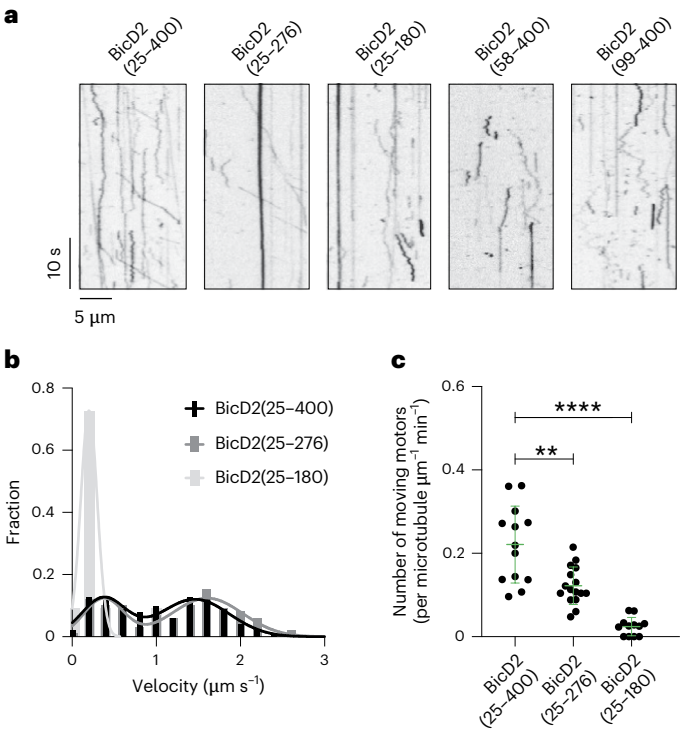

Fig. 4 | Motility of DDB complexes assembled with BicD2 constructs of varying lengths. a, Example kymographs of DDB complexes with different BicD2 constructs. **b**, Velocity histograms. BicD2(25–400) and BicD2(25–276) fit to two Gaussians; BicD2(25–180) fits to one. BicD(25–400), 0.37 ± 0.26 and 1.46 ± 0.41 µm s^{-1} (n = 102); BicD(25–276), 0.23 ± 0.12 and 1.60 ± 0.42 µm s^{-1} (n = 100); BicD(25–180), 0.20 ± 0.10 µm s^{-1} (n = 11). The single low-velocity peak for BicD(25–180) indicates its inability to recruit two dyneins. **c**, Number of moving motors (mean ± s.d.): BicD2(25–400), 0.22 ± 0.09 (n = 13); BicD2(25–276), 0.12 ± 0.04 (n = 16) and BicD2(25–180), 0.02 ± 0.02 (n = 12). Two-tailed unpaired Student's t-test with Welch's correction; ****P < 0.0001, **P = 0.0026.

whereas BicD2(25–180) extends only to the position occupied by the middle dynein (dynein-A; ref. 43; Fig. 3f). Using single-molecule fluorescence and optical-tweezers assays, we assessed the functionality of these constructs. BicD2(25–276) formed DDB complexes capable of motion and force generation (Fig. 4a and Extended Data Fig. 2e), similar to BicD2(25–400) (Fig. 1b). In contrast, the shortest construct, BicD2(25–180), not only failed to form DDB complexes with two dyneins (D_2DB; Fig. 4b) but also formed significantly fewer complexes with one dynein (D_1DB; Fig. 4b,c), generating forces of only about 2.5 or 4.5 pN (Extended Data Fig. 2f). These results indicate that BicD2 must span the full dynactin shoulder to form and stabilize DDB complexes but they leave open the question of whether it directly participates in the binding of the third dynein.

A recent cryo-EM study revealed that a second BICDR1 molecule (BICDR-B) can stabilize the microtubule-bound DDR complex by acting as an auxiliary adaptor[72] (Figs. 1a and 3c,f). Although a second BicD2 molecule has not yet been visualized in DDB cryo-EM structures[42], we investigated the possibility that a second auxiliary BicD2 adaptor facilitates the recruitment of the third dynein by employing the shortest construct, BicD2(25–180), without a biotinylated carboxy terminus. This modified construct, which is incapable of binding to streptavidin beads or forming functional DDB complexes on its own, retains the segment capable of interacting with pre-assembled DDB complexes that include BicD2(25–400) anchored to streptavidin beads (Fig. 3f). When 5 nM excess dynein and BicD2(25–180) were added to pre-assembled DDB complexes, we observed dominant 9-pN forces in approximately 60% of all force-generating beads (Fig. 3a and Extended Data Fig. 2g; increase in 9-pN fraction; DDB + dynein versus DDB + dynein + BicD2(25–180), P = 0.008). These results strongly suggest that a second auxiliary BicD2 adaptor plays a critical role in recruiting a third dynein.

Further insights into this interaction came from cryo-EM structures of DDR complexes with two BICDR1 molecules[44] (Figs. 1a and 3f). The CC1 box (AAxxG, where x indicates any amino acid) of the N terminus of the primary BICDR1 (BICDR-A) interacts with α-helix-1 of the C terminus of the LIC from dynein B (B1)[44] and with the LIC of dynein-A (A2; Fig. 3f,g). Consistent with a functional role for this interaction, removal of the BicD2 N terminus completely abolished DDB-complex formation (Fig. 4a). In contrast, the second auxiliary BICDR1 (BICDR-B) N terminus interacts exclusively with the LIC of dynein A2 (ref. 44). Although the LIC of dynein A2 interacts with both BICDR-A and BICDR-B[44], the unoccupied surface of the latter may bind the LIC of the third dynein.

To directly assess whether recruitment is impaired by disrupting the interaction between the auxiliary BicD2 and the LIC of the third dynein, we introduced a single-point mutation (Y46D) in BicD2(25–180). This mutation disrupts the hydrophobic interaction between the BicD2 N terminus and the dynein LIC[73]. When 5 nM mutated BicD2(25–180, Y46D) and 5 nM free dynein were added to pre-assembled DDB complexes, we observed a significant reduction in force generation, with fewer than 13% of beads producing 9-pN forces (Fig. 3a; reduction in 9-pN fraction versus BicD2(25–180), P < 0.001). These findings demonstrate that recruitment of the third dynein critically depends on the interaction between the second auxiliary BicD2 and the LIC of the third dynein.

Tension-induced recruitment of a third dynein to DDB complexes

A key question is why cryo-EM and cryogenic electron tomography studies have not reported a third dynein bound to DDB, despite our evidence for its functional contribution. This is most probably a result of in the experimental conditions: unlike static structural approaches, our optical-trapping assay applies mechanical load to DDB complexes. Under these conditions, we observed step-like increases in stalling forces (Fig. 1d), suggesting that tension can facilitate the recruitment of additional dyneins[74], enabling the complex to adapt to elevated force demands.

To directly test this idea, we engineered a DDB–rigor kinesin chimaera by covalently linking a DDB complex to a truncated kinesin-1 rigor mutant (KIF5B(1–490))[75] via BicD2, using the SpyTag–SpyCatcher system[76]. SpyCatcher (SpyCatcher003)[77] was inserted at the C terminus of BicD2 and SpyTag (SpyTag003)[77] was fused to the C terminus of the kinesin mutant (Fig. 5a). This rigor kinesin binds strongly to microtubules but is immotile[75], thereby serving as a static anchor. The SpyTag–SpyCatcher reaction covalently conjugated BicD2 with rigor kinesin in a 2:2 stoichiometry, as confirmed by mass spectrometry (Fig. 5b). Control experiments established that BicD2 did not bind either the truncated kinesin or the microtubules on its own (Fig. 5c,d) and that co-localization with microtubules occurred only when BicD2 was covalently linked to rigor kinesin (Fig. 5e).

In this chimaera the kinesin motor domains tether the complex to the microtubule while the DDB complex simultaneously engages the lattice. For minus-end-directed movement to occur, DDB must generate sufficient force to overcome the strong microtubule binding of the rigor kinesin. This load state provides a mechanism by which backwards tension promotes recruitment of a third dynein.

We tested this hypothesis using three-colour single-molecule total internal reflection fluorescence (TIRF) microscopy. DDB–rigor kinesin complexes were pre-assembled with three differently labelled dyneins (Alexa Fluor 488, tetramethylrhodamine (TMR) and Alexa Fluor 647 dyes) in a 3:1:1 ratio (dynein:dynactin:BicD2–rigor kinesin) and introduced into slide chambers containing 10 nM of either BicD2(25–180) or its mutant BicD2(25–180, Y46D) in the presence of

https://doi.org/10.1038/s41556-026-01877-0

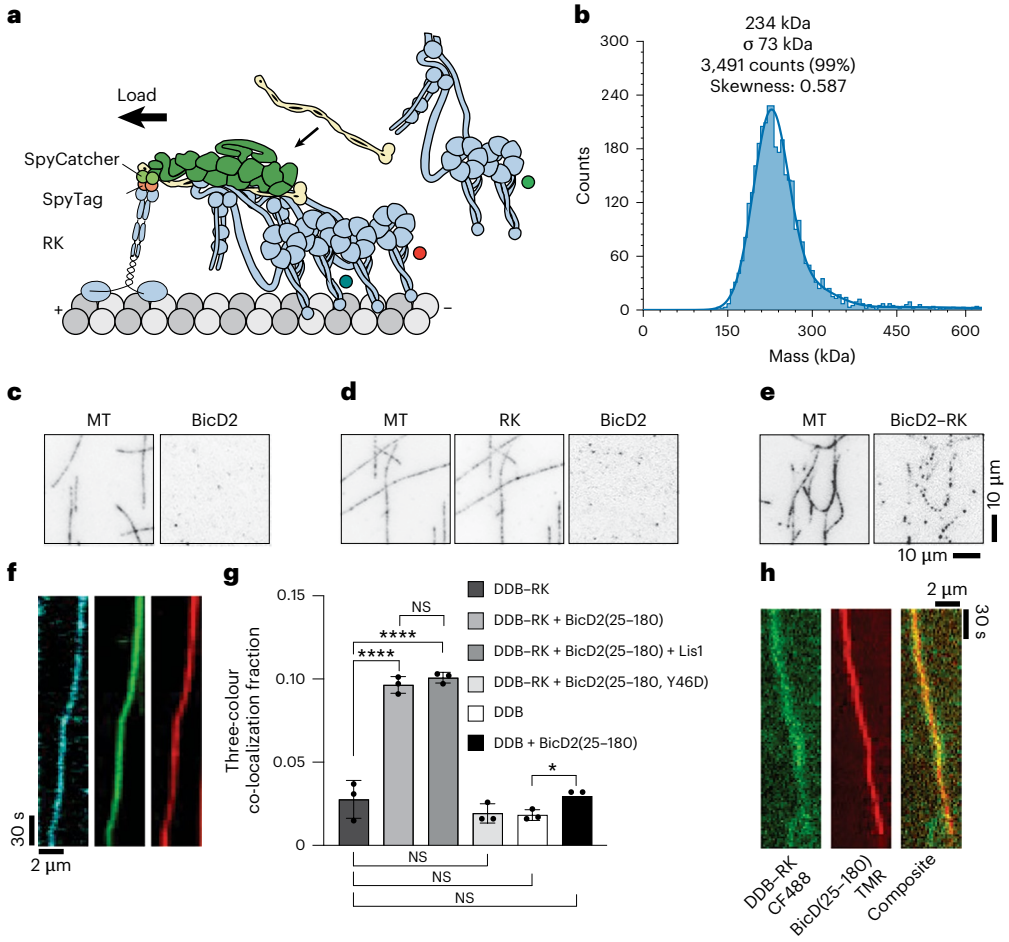

Fig. 5 | DDB–rigor kinesin complexes associate with three dyneins. **a**, Schematic of KIF5B(1–490) covalently linked to BicD2 in the DDB complex via SpyTag–SpyCatcher. **b**, Mass photometry reveals a 234-kDa species corresponding to a BicD2(25–400) dimer (56.3 kDa monomer) bound to truncated rigor kinesin dimer (58.5 kDa monomer). **c**, Cyanine 3-labelled BicD2(25–400) does not bind microtubules. **d**, Cyanine 5-labelled rigor kinesin binds microtubules but does not recruit cyanine 3–BicD2(25–400). **e**, BicD2–rigor kinesin conjugates (cyanine 5–BicD2(25–400)) co-localize with microtubules. **f**, Kymographs showing DDB–rigor kinesin complexes with three fluorescently labelled dyneins moving along microtubules at 100 µM ATPγS (cyan, Alexa Fluor 488; green, TMR; red, Alexa Fluor 647). **g**, Frequencies of three-colour dynein co-localization (mean ± s.d.): DDB–rigor kinesin, 0.028 ± 0.011 (replicates (r) = 3, n = 616 total molecules); DDB–rigor kinesin + BicD2(25–180), 0.096 ± 0.005 (r = 3, n = 596); DDB–rigor kinesin + BicD2(25–180) + Lis1, 0.101 ± 0.003 (r = 3, n = 485); DDB–rigor kinesin + BicD2(25–180, Y46D), 0.019 ± 0.006 (r = 3, n = 570); DDB, 0.018 ± 0.003 (r = 3, n = 793); and DDB + BicD2(25–180), 0.030 ± 0.004 (r = 3, n = 675). One-way analysis of variance with Dunnett's test; ****P < 0.0001; NS, not significant (P = 0.37, 0.28 and 0.99 for DDB–rigor kinesin + BicD2(25–180, Y46D), DDB and DDB + BicD2(25–180), respectively). Two-tailed unpaired Student's t-test with Welch's correction; DDB–rigor kinesin + BicD2(25–180) versus DDB–rigor kinesin + BicD2(25–180) + Lis1; NS (P = 0.29); DDB versus DDB + BicD2(25–180), *P = 0.02. **h**, Trace showing co-localization of TMR–BicD2(25–180) and CF488–rigor kinesin conjugated to BicD2(25–400) moving along microtubules at 100 µM ATPγS. RK, rigor kinesin.

100 µM ATPγS to prolong microtubule binding. Under these conditions, the addition of BicD2(25–180) significantly increased the fraction of three-colour co-localizations (Fig. 5f,g and Extended Data Fig. 3), whereas the Y46D mutant had no effect (Fig. 5g), providing support for the role of the BicD2–LIC interaction in third-dynein recruitment. Lis1 did not further enhance three-colour co-localizations in the presence of extra BicD2(25–180) (Fig. 5g), suggesting that auxiliary BicD2 plays a dominant role. By contrast, only a slight increase was observed for DDB complexes lacking rigor kinesin in three-colour co-localizations with BicD2(25–180) (Fig. 5g), highlighting that backwards tension is critical for efficient recruitment of a third dynein. Notably, the increased frequency of the three-dynein complexes under these conditions correlates with the higher fraction of 9-pN stalling forces observed in optical-trapping experiments (Fig. 3a).

To complement the functional assays, we also attempted to directly visualize two BicD2 molecules in the same complex. Because high concentrations of fluorescently labelled BicD2 introduce substantial background fluorescence, such experiments are technically challenging. Nonetheless, when 10 nM auxiliary TMR-labelled BicD2(25–180) was added to DDB–rigor kinesin complexes in which the rigor kinesin (CF488-labelled) was covalently linked to the primary BicD2(25–400) via the SpyTag–SpyCatcher system, we occasionally observed co-movement of both fluorophores along microtubules (Fig. 5h and Extended Data Fig. 4). Although rare—we detected 1–2 co-localized moving molecules per peripheral region of the field of view where the background intensity was sufficiently low (details in Methods)—these events are consistent with the simultaneous association of two BicD2 molecules in the same complex. The low apparent frequency probably reflects technical constraints: CF488 photobleaching frequently leads to signal loss before movement becomes apparent and the 10 nM TMR–BicD2 concentration required for visualization of DDB–rigor kinesin complexes with the TMR-labelled accessory adaptor generates background levels that prevent detection across most of the field of view. However, together with the strong reduction of 9-pN forces following the addition of BicD2(25–180, Y46D), these observations provide supportive evidence for the two-adaptor model.

https://doi.org/10.1038/s41556-026-01877-0

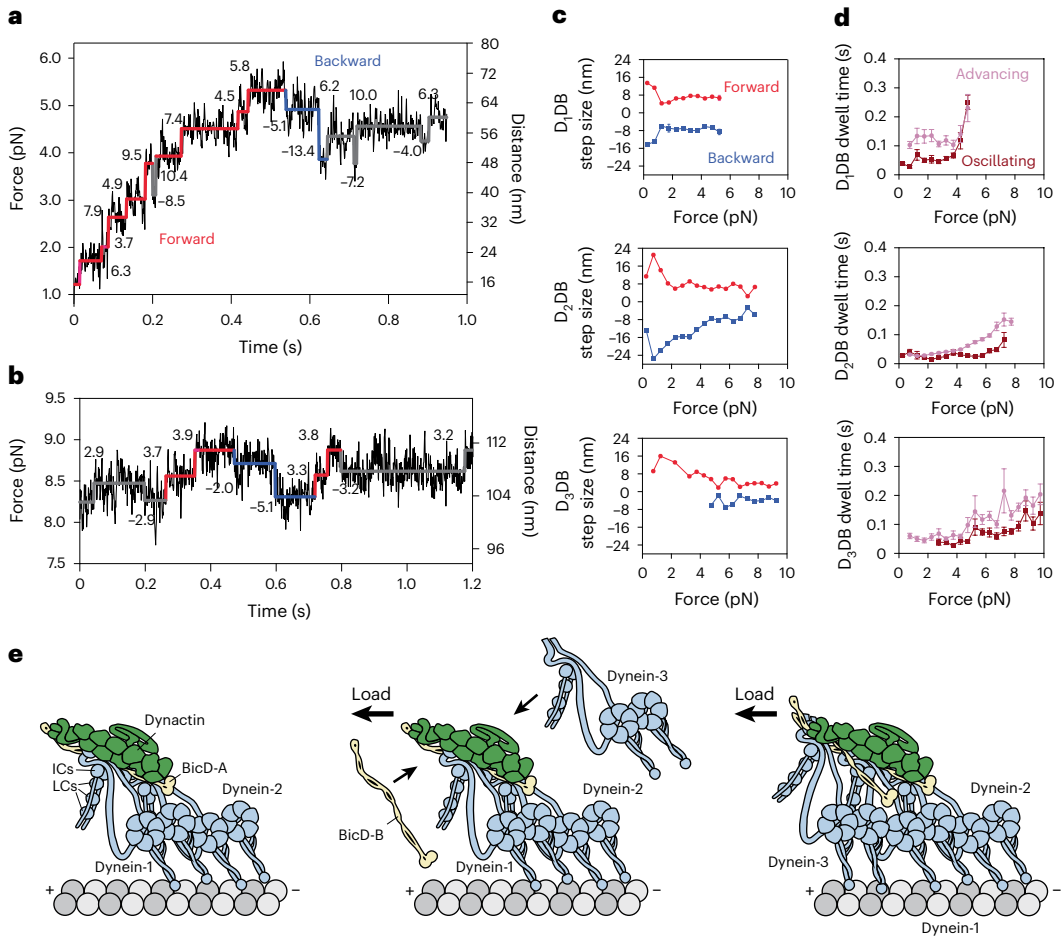

Fig. 6 | Force-dependent stepping behaviour of DDB complexes. **a**,**b**, Representative traces of D_2DB (**a**) and D_3DB (**b**) showing stepwise displacements. Advancing forward and backward steps, and oscillatory forward–backward steps, are shown in red, blue and grey, respectively. **c**, Step sizes of advancing DDB complexes as a function of load. Forward and backward steps were binned in 0.5-pN windows; **d**, Dwell times preceding forward steps in advancing and oscillatory modes, binned in 0.5-pN windows. Two-tailed paired Sudent's *t*-test: D_1DB: $^{**}P = 0.0016$; D_2DB: $^{**}P = 0.0016$; D_3DB: $^{****}P < 0.0001$. **c**,**d**, Number of beads at each stall force: D_1DB, $n = 12$ (top); D_2DB, $n = 16$ (middle); and D_3DB, $n = 10$. Points represent the mean ± s.e.m. (error bars smaller than the symbols are not visible). **e**, Model for tension-induced recruitment of a third dynein to DDB via BicD2 (dynactin p150 omitted). Under backward load, an additional BicD2 adaptor enables recruitment of a third dynein, increasing force output. This model is supported by the data in Figs. 3–5 showing load-dependent third-dynein recruitment and enhanced force generation. LCs and ICs, light and intermediate chains.

In conclusion, these results demonstrate that mechanical load promotes recruitment of a third dynein to DDB complexes through an auxiliary BicD2 adaptor. This load-induced adaptation enhances both force output and motility, enabling DDB complexes to dynamically respond to escalating mechanical demands.

DDB exhibits predominantly load-independent 8-nm steps along microtubules

Cryogenic electron microscopy studies suggest that the motor domains of the two dyneins engaged within DDB complexes adopt a compact parallel arrangement[42], which would predict smaller centre-of-mass displacements along microtubules. In contrast, single-molecule fluorescence experiments have reported highly variable step sizes, ranging from 4 to 48 nm, in unloaded conditions[19,62]. Optical-trapping studies further demonstrated that the mean forward step sizes decrease with increasing load, from approximately 15 nm at 0.4 pN (range, 4–32 nm) to 10 nm at 3.6 pN (range, 2–28 nm)[62]. Given the structural arrangement of the dynein motor domains[42], step sizes as large as 48 nm would require substantial rearrangements of the motor domains, making such displacements unlikely.

In our experiments DDB complexes primarily took small steps (Fig. 6a,b). For DDB bound to a single dynein (D_1DB), forward movements under loads of >1 pN consisted almost exclusively of 8-nm steps (Fig. 6c(top), red), even after correcting for the complex's compliance (Extended Data Fig. 5a). At lower loads occasional consecutive forward steps reached about 16 nm (Fig. 6c(top), red). For DDB complexes with two dyneins (D_2DB), the step sizes remained centred around 8 nm under loads of >2 pN (Fig. 6a,c(middle), red), with occasional steps of up to 24 nm at low load (Fig. 6c(middle), red). These results are consistent with earlier step-size measurements in the absence of load[19,62]. By contrast, when DDB contained three dyneins (D_3DB), the step sizes were smaller than those of D_1DB and D_2DB (Fig. 6b,c(bottom), red), indicating that the third dynein alters both the stepping behaviour and the overall velocity (Extended Data Fig. 5b).

Backward and oscillatory forward–backward steps revealed additional load-dependent behaviours (Fig. 6c). For D_1DB, the backward steps were similar in size to forward steps (Fig. 6c(top), blue). In contrast, D_2DB displayed larger backward step sizes under loads of <4 pN (Fig. 6c(middle), blue), suggesting that its two dynein dimers can separate more widely at low load—potentially resynchronizing the motors if one advances too far ahead. D_3DB, however, showed almost no backward stepping under low-load conditions (Fig. 6c(bottom), blue), consistent with at least two dimers remaining bound to the microtubule

at any time. In addition to these advancing and backward steps, all DDB complexes exhibited an oscillatory forward–backward stepping mode reminiscent of *S. cerevisiae* dynein[78] (Fig. 6a,b, grey) in which a backward step was rapidly followed by a forward step. Step sizes in this mode were comparable to advancing steps (Fig. 6c and Extended Data Fig. 6a) but dwell-time analyses distinguished them: the dwell times between advancing forward steps increased with increasing load (Fig. 6d, pink), whereas forward steps during the oscillatory forward–backward stepping mode were preceded by shorter load-insensitive dwells (Fig. 6d, dark red, and Extended Data Fig. 6b,c). This results in a relative constant dwell time that is insensitive to forces below the substalling force for oscillatory forward–backward stepping. This behaviour indicates that unlike the ordered hand-over-hand mechanism of kinesin-1, DDB steps more stochastically, resembling *S. cerevisiae* dynein[71,78–80], in which the leading motor domain can detach and rapidly rebind in a forward position.

Together, these analyses reveal that DDB complexes predominantly move in centre-of-mass displacements of about 8 nm under substall loads, consistent with a compact motor arrangement. Under near-unloaded conditions, DDB complexes exhibit their full range of step sizes, extending up to 24 nm, whereas near stall loads restrict stepping to increments as small as 4 nm. This behaviour suggests that the motor domains remain coordinated under load but adopt greater flexibility under low load. Such dynamic switching highlights the ability of DDB complexes to adjust their stepping mechanics to meet varying mechanical demands[74].

Discussion

Our study revealed a mechanosensitive property of DDB motor complexes: under increasing load, additional dyneins are recruited, enhancing force production and processivity. Using recombinant reconstitution, structural analysis, optical-trapping and multicolour single-molecule imaging, we demonstrated that mechanical tension promotes higher-order DDB assembly. These findings expand our understanding of how dynein adapts to mechanical demands during intracellular transport and uncover a load-dependent mechanism of motor recruitment and coordination (Fig. 6e).

Dynein force generation is limited by an autoinhibitory phi-like conformation

Optical-trapping studies show that mammalian dynein alone generates approximately 1 pN in weak traps (stiffness, 0.01 pN nm^{-1})[40,53,81], with occasional reports of 7–8 pN (refs. 82,83) and 2 pN at higher trap stiffness (0.1 pN nm^{-1})[40], reflecting low processivity. In contrast, *S. cerevisiae* dynein, which is highly processive, displays a trap stiffness-independent stall force of 4.5 pN (ref. 40). D_1DB complexes stall at 2.5 pN (trap stiffness, 0.06 pN nm^{-1}), matching isolated human dynein[40,61] and suggesting that force output is limited by an autoinhibitory phi-like conformation in which one motor domain ceases forward stepping. Although autoinhibited dynein binds microtubules weakly[50], a nucleotide-free AAA1 state can form a strong force-insensitive ideal bond[63,84,85], while the detached head attempts to cross its stalk over the bound partner, generating the phi-like conformation.

Mutations preventing autoinhibition provided support for this mechanism: D_1DB complexes with these mutations exclusively generate forces of 4.5 pN. Lis1 similarly stabilized the active state, strongly reducing 2.5-pN stalls and shifting force output to 4.5 pN (Fig. 2c). Higher trap stiffness activates dynein as well[40], indicating that load alone can overcome autoinhibition. Fission yeast dynein, functional without Lis1 (ref. 47), fits this model. D^{act}DB complexes, which cannot autoinhibit[50], predominantly formed two-dynein assemblies (D_2DB) that stalled at 7 pN, probably because open conformations favour recruitment and LIC–motor domain contacts stabilize these assemblies[44]. Thus, both Lis1 and load prevent autoinhibition to increase force and processivity.

Tension-induced dynein recruitment

DDB complexes recruit a third dynein under increasing load, raising stall forces to 9 pN. Recruitment requires an auxiliary BicD2 adaptor that engages the LIC of the third dynein, as shown by reduced recruitment in the BicD2(Y46D) mutant. The auxiliary BICDR1 in DDR probably fulfills the same role. Cryogenic electron tomography[42] and cryo-EM[37] structures describe assemblies with one adaptor and one or occasionally two dyneins[42,43]; here we identified mechanical tension as the factor enabling addition of a third dynein. The resulting increase in force probably allows DDB to overcome cytoplasmic resistance during demanding transport events[86].

Three-dynein recruitment occurs when DDB opposes a rigor kinesin but not in its absence. Although the precise loading rate is unknown, the observed motion (Extended Data Fig. 5b) indicated that D_3DB generates >7 pN, which is sufficient to unbind kinesin from the microtubule[87]. Continuous minus-end-directed movement of D_3DB–rigor kinesin complexes (Fig. 5f) implies repeated kinesin detachment and rebinding as DDB advances. Dual-BicD2 co-localization events provided visual support for the two-adaptor model (Fig. 5h). Together with the Y46D mutation, these observations provide support for auxiliary adaptor–mediated recruitment of the third dynein (Fig. 6e).

Lis1 further promotes higher-order assembly when competing with kinesin-1 under load[19]. Without Lis1, only approximately 20% of DDB complexes contained two dyneins and stall at 4.1 pN, which is insufficient to oppose the stall force of kinesin-1 (5–6 pN)[40,88–90]. Lis1 increases two-dynein assemblies to about 40% and raises the stall force to 5.4 pN (ref. 19). Under these conditions, approximately 20% of kinesin–DDB complexes showed dynein-directed movement, probably reflecting recruitment of a third dynein[19]. A related study[91] found that tethering DDB to KIF1C increased processivity by 50%. Because KIF1C generates forces up to 7 pN (ref. 92), recruiting a third dynein (9 pN) is likely to be necessary to overcome KIF1C. Thus, load and Lis1 cooperatively promote higher-order dynein assembly.

Mechanism of load-induced recruitment

A plausible mechanism for this load-induced recruitment is that backward tension on the BicD2 C terminus (cargo-proximal end) is transmitted through the coiled-coil to dynactin, inducing allosteric changes that favour binding of a second (auxiliary) BicD2 and, in turn, a third dynein. Load may stabilize a coiled-coil registry shift in the primary BicD2, similar to the cargo-induced shift thought to relieve autoinhibition[93–97], thereby exposing additional acidic or charged patches that promote auxiliary BicD2 association and recruitment of a third dynein tail via LIC interactions. Alternatively, load may propagate into dynactin's shoulder and Arp1 lattice[98], subtly altering the dynein tail geometry to increase the likelihood that an auxiliary adaptor engages near an adjacent tail. Tension could also modulate the LIC–adaptor interaction directly, either by reducing competition from alternative binding sites or by increasing affinity, thus favouring auxiliary BicD2 capture. Together, these scenarios explain how load could gate adaptor binding and third-dynein recruitment—a model supported by our observation that backward load enhances both the frequency of three-colour events and 9-pN force states, consistent with force-gated dynein assembly in vivo[74].

Dyneins share load unequally through a staggered arrangement

Our results indicate that dyneins in DDB complexes share load unequally. The leading dynein typically slows near its stall force (approximately 4.5 pN), triggering the engagement of additional motors and stepwise increases to around 7 or 9 pN. This suggests sequential engagement as load rises (Fig. 1d). Although cryo-electron tomography shows all four motor domains aligned in parallel[42], the 40° angle of the dynactin shoulder relative to the microtubule axis implies offset microtubule-binding sites under physiological load. In

this configuration, tension at the BicD2 C terminus would align the shoulder with the microtubule axis, producing a staggered motor arrangement. Such a geometry enforces unequal load sharing, consistent with observed force increments of 2.5 pN per additional dynein. This model is supported by DNA-origami scaffolds that bind two or three D_1DB complexes in a staggered configuration, which yield stall forces of approximately 7 and 9 pN (ref. 62). Thus, multiple dyneins collectively generate force but load distribution among them is inherently unequal.

DDB primarily moves in 8-nm steps under load

After correcting for force-dependent compliance (Extended Data Fig. 5a and Methods), DDB complexes were found to predominantly take 8-nm centre-of-mass steps under loads of >2 pN (Fig. 6a,c). The step size remained largely load-independent for D_1DB and D_2DB, whereas D_3DB exhibited smaller (approximately 4 nm) steps near stall forces (Fig. 6b,c), reminiscent of *S. cerevisiae* dynein near stall force[78]. Previously reported 10-nm steps at 3.6 pN load (step sizes ranging from 2 to 28 nm)[62] may reflect underfitting by earlier step-detection algorithms or effects of axonemal substrates containing co-purified proteins[64,65]. Our automated detection avoids underfitting and resolves smaller increments.

D_3DB complexes also moved more slowly than D_2DB under loads of up to 5 pN (Extended Data Fig. 5b), probably because the third perturbs coordination. The third motor may bear less load and step ahead, disrupting optimal spacing, while LIC–motor–domain interactions between leading and trailing dyneins[72] may promote coordination in D_2DB but not D_3DB. These factors could explain the reduced step sizes and velocity observed for D_3DB complexes. Backward step sizes mirrored forward step sizes (Fig. 6c), consistent with a reversal of previous forward steps.

We also observed forward–backward stepping reminiscent of MINFLUX studies of *S. cerevisiae* dynein[99], characterized by short dwell times and limited load dependence. These probably reflect ATP-driven recovery movements after load-induced detachment. We propose that the detached head undergoes a load-induced backward displacement and, after ATP binding (both events possibly influenced by load) moves forward again through a priming stroke of its linker. Correlative force and single-molecule fluorescence measurements will be needed to confirm this mechanism.

In conclusion, dynein–dynactin complexes adapt to mechanical load by recruiting additional motors, redistributing force and tuning their stepping behaviour to ensure robust intracellular transport (Fig. 6e).

Online content

Any methods, additional references, Nature Portfolio reporting summaries, source data, extended data, supplementary information, acknowledgements, peer review information; details of author contributions and competing interests; and statements of data and code availability are available at https://doi.org/10.1038/s41556-026-01877-0.

References

1. Abe, T. K. et al. Dynactin is essential for growth cone advance. *Biochem. Biophys. Res. Commun.* **372**, 418–422 (2008).
2. Grabham, P. W., Seale, G. E., Bennecib, M., Goldberg, D. J. & Vallee, R. B. Cytoplasmic dynein and LIS1 are required for microtubule advance during growth cone remodeling and fast axonal outgrowth. *J. Neurosci.* **27**, 5823–5834 (2007).
3. Tai, C. Y., Dujardin, D. L., Faulkner, N. E. & Vallee, R. B. Role of dynein, dynactin, and CLIP-170 interactions in LIS1 kinetochore function. *J. Cell Biol.* **156**, 959–968 (2002).
4. Vallee, R. B., Williams, J. C., Varma, D. & Barnhart, L. E. Dynein: an ancient motor protein involved in multiple modes of transport. *J. Neurobiol.* **58**, 189–200 (2004).
5. Kardon, J. R. & Vale, R. D. Regulators of the cytoplasmic dynein motor. *Nat. Rev. Mol. Cell Biol.* **10**, 854–865 (2009).
6. Yamada, M. et al. LIS1 and NDEL1 coordinate the plus-end-directed transport of cytoplasmic dynein. *EMBO J.* **27**, 2471–2483 (2008).
7. Tsai, J. W., Chen, Y., Kriegstein, A. R. & Vallee, R. B. LIS1 RNA interference blocks neural stem cell division, morphogenesis, and motility at multiple stages. *J. Cell Biol.* **170**, 935–945 (2005).
8. Vallee, R. B., Tai, C. & Faulkner, N. E. LIS1: cellular function of a disease-causing gene. *Trends Cell Biol.* **11**, 155–160 (2001).
9. Feng, Y. & Walsh, C. A. Protein–protein interactions, cytoskeletal regulation and neuronal migration. *Nat. Rev. Neurosci.* **2**, 408–416 (2001).
10. Cahana, A. et al. Targeted mutagenesis of Lis1 disrupts cortical development and LIS1 homodimerization. *Proc. Natl. Acad. Sci. USA* **98**, 6429–6434 (2001).
11. Feng, Y. & Walsh, C. A. Mitotic spindle regulation by Nde1 controls cerebral cortical size. *Neuron* **44**, 279–293 (2004).
12. Pawlisz, A. S. et al. Lis1–Nde1-dependent neuronal fate control determines cerebral cortical size and lamination. *Hum. Mol. Genet.* **17**, 2441–2455 (2008).
13. Reiner, O. et al. Lissencephaly gene (LIS1) expression in the CNS suggests a role in neuronal migration. *J. Neurosci.* **15**, 3730–3738 (1995).
14. Mochida, G. H. Genetics and biology of microcephaly and lissencephaly. *Semin. Pediatr. Neurol.* **16**, 120–126 (2009).
15. Leventer, R. in *Handbook of Clinical Neurology*, Vol. 87 (eds Sarnat, H. & Curtaolo, P.) 205–218 (Elsevier, 2008).
16. Kato, M. & Dobyns, W. B. Lissencephaly and the molecular basis of neuronal migration. *Hum. Mol. Genet.* **12**, R89–R96 (2003).
17. Wynshaw-Boris, A. Lissencephaly and LIS1: insights into the molecular mechanisms of neuronal migration and development. *Clin. Genet.* **72**, 296–304 (2007).
18. Tanaka, T. et al. Lis1 and doublecortin function with dynein to mediate coupling of the nucleus to the centrosome in neuronal migration. *J. Cell Biol.* **165**, 709–721 (2004).
19. Elshenawy, M. M. et al. Lis1 activates dynein motility by modulating its pairing with dynactin. *Nat. Cell Biol.* **22**, 570–578 (2020).
20. King, S. J. & Schroer, T. A. Dynactin increases the processivity of the cytoplasmic dynein motor. *Nat. Cell Biol.* **2**, 20–24 (2000).
21. Schroer, T. A. Dynactin. *Annu. Rev. Cell Dev. Biol.* **20**, 759–779 (2004).
22. McKenney, R. J., Huynh, W., Tanenbaum, M. E., Bhabha, G. & Vale, R. D. Activation of cytoplasmic dynein motility by dynactin–cargo adapter complexes. *Science* **345**, 337–341 (2014).
23. Schlager, M. A., Hoang, H. T., Urnavicius, L., Bullock, S. L. & Carter, A. P. In vitro reconstitution of a highly processive recombinant human dynein complex. *EMBO J.* **33**, 1855–1868 (2014).
24. Kardon, J. R., Reck-Peterson, S. L. & Vale, R. D. Regulation of the processivity and intracellular localization of *Saccharomyces cerevisiae* dynein by dynactin. *Proc. Natl. Acad. Sci. USA* **106**, 5669–5674 (2009).
25. Moughamian, A. J. & Holzbaur, E. L. F. Dynactin is required for transport initiation from the distal axon. *Neuron* **74**, 331–343 (2012).
26. Tripathy, S. K. et al. Autoregulatory mechanism for dynactin control of processive and diffusive dynein transport. *Nat. Cell Biol.* **16**, 1192–1201 (2014).
27. Ross, J. L., Wallace, K., Shuman, H., Goldman, Y. E. & Holzbaur, E. L. Processive bidirectional motion of dynein–dynactin complexes in vitro. *Nat. Cell Biol.* **8**, 562–570 (2006).
28. Nirschl, J. J., Magiera, M. M., Lazarus, J. E., Janke, C. & Holzbaur, E. L. α-Tubulin tyrosination and CLIP-170 phosphorylation regulate the initiation of dynein-driven transport in neurons. *Cell Rep.* **14**, 2637–2652 (2016).

29. McKenney, R. J., Huynh, W., Vale, R. D. & Sirajuddin, M. Tyrosination of α-tubulin controls the initiation of processive dynein–dynactin motility. *EMBO J.* **35**, 1175–1185 (2016).
30. Ayloo, S. et al. Dynactin functions as both a dynamic tether and brake during dynein-driven motility. *Nat. Commun.* **5**, 4807 (2014).
31. Cianfrocco, M. A., DeSantis, M. E., Leschziner, A. E. & Reck-Peterson, S. L. Mechanism and regulation of cytoplasmic dynein. *Annu. Rev. Cell Dev. Biol.* **31**, 83–108 (2015).
32. Qiu, R., Zhang, J. & Xiang, X. p25 of the dynactin complex plays a dual role in cargo binding and dynactin regulation. *J. Biol. Chem.* **293**, 15606–15619 (2018).
33. Munch, C. et al. Point mutations of the p150 subunit of dynactin (*DCTN1*) gene in ALS. *Neurology* **63**, 724–726 (2004).
34. Puls, I. et al. Mutant dynactin in motor neuron disease. *Nat. Genet.* **33**, 455–456 (2003).
35. Farrer, M. J. et al. DCTN1 mutations in Perry syndrome. *Nat. Genet.* **41**, 163–165 (2009).
36. Chowdhury, S., Ketcham, S. A., Schroer, T. A. & Lander, G. C. Structural organization of the dynein–dynactin complex bound to microtubules. *Nat. Struct. Mol. Biol.* **22**, 345–347 (2015).
37. Urnavicius, L. et al. The structure of the dynactin complex and its interaction with dynein. *Science* **347**, 1441–1446 (2015).
38. Trokter, M., Mücke, N. & Surrey, T. Reconstitution of the human cytoplasmic dynein complex. *Proc. Natl. Acad. Sci. USA* **109**, 20895–20900 (2012).
39. Nicholas, M. P. et al. Control of cytoplasmic dynein force production and processivity by its C-terminal domain. *Nat. Commun.* **6**, 6206 (2015).
40. Brenner, S., Berger, F., Rao, L., Nicholas, M. P. & Gennerich, A. Force production of human cytoplasmic dynein is limited by its processivity. *Sci. Adv.* **6**, eaaz4295 (2020).
41. Olenick, M. A., Tokito, M., Boczkowska, M., Dominguez, R. & Holzbaur, E. L. Hook adaptors induce unidirectional processive motility by enhancing the dynein–dynactin interaction. *J. Biol. Chem.* **291**, 18239–18251 (2016).
42. Grotjahn, D. A. et al. Cryo-electron tomography reveals that dynactin recruits a team of dyneins for processive motility. *Nat. Struct. Mol. Biol.* **25**, 203–207 (2018).
43. Urnavicius, L. et al. Cryo-EM shows how dynactin recruits two dyneins for faster movement. *Nature* **554**, 202–206 (2018).
44. Chaaban, S. & Carter, A. P. Structure of dynein–dynactin on microtubules shows tandem adaptor binding. *Nature* **610**, 212–216 (2022).
45. Toropova, K. et al. Lis1 regulates dynein by sterically blocking its mechanochemical cycle. *eLife* **3**, e03372 (2014).
46. Huang, J., Roberts, A. J., Leschziner, A. E. & Reck-Peterson, S. L. Lis1 acts as a "clutch" between the ATPase and microtubule-binding domains of the dynein motor. *Cell* **150**, 975–986 (2012).
47. DeSantis, M. E. et al. Lis1 has two opposing modes of regulating cytoplasmic dynein. *Cell* **170**, 1197–1208 (2017).
48. Marzo, M. G., Griswold, J. M. & Markus, S. M. Pac1/LIS1 stabilizes an uninhibited conformation of dynein to coordinate its localization and activity. *Nat. Cell Biol.* **22**, 559–569 (2020).
49. Qiu, R., Zhang, J. & Xiang, X. LIS1 regulates cargo–adapter-mediated activation of dynein by overcoming its autoinhibition in vivo. *J. Cell Biol.* **218**, 3630–3646 (2019).
50. Zhang, K. et al. Cryo-EM reveals how human cytoplasmic dynein is auto-inhibited and activated. *Cell* **169**, 1303–1314 (2017).
51. Amos, L. A. Brain dynein crossbridges microtubules into bundles. *J. Cell Sci.* **93**, 19–28 (1989).
52. Toropova, K., Mladenov, M. & Roberts, A. J. Intraflagellar transport dynein is autoinhibited by trapping of its mechanical and track-binding elements. *Nat. Struct. Mol. Biol.* **24**, 461–468 (2017).
53. Torisawa, T. et al. Autoinhibition and cooperative activation mechanisms of cytoplasmic dynein. *Nat. Cell Biol.* **16**, 1118–1124 (2014).
54. Geohring, I. C. et al. A nucleotide code governs Lis1's ability to relieve dynein autoinhibition. *Nat. Chem. Biol.* https://doi.org/10.1038/s41589-025-02096-8 (2026).
55. Jordan, M. A., Diener, D. R., Stepanek, L. & Pigino, G. The cryo-EM structure of intraflagellar transport trains reveals how dynein is inactivated to ensure unidirectional anterograde movement in cilia. *Nat. Cell Biol.* **20**, 1250–1255 (2018).
56. Chai, P. et al. The mechanochemical cycle of reactive full-length human dynein 1. *Nat. Struct. Mol. Biol.* **32**, 1383–1395 (2025).
57. Htet, Z. M. et al. LIS1 promotes the formation of activated cytoplasmic dynein-1 complexes. *Nat. Cell Biol.* **22**, 518–525 (2020).
58. Ton, W. D. et al. Microtubule-binding-induced allostery triggers LIS1 dissociation from dynein prior to cargo transport. *Nat. Struct. Mol. Biol.* **30**, 1365–1379 (2023).
59. Singh, K. et al. Molecular mechanism of dynein–dynactin complex assembly by LIS1. *Science* **383**, eadk8544 (2024).
60. Nicastro, D. et al. Cryo-electron tomography reveals conserved features of doublet microtubules in flagella. *Proc. Natl Acad. Sci. USA* **108**, E845–E853 (2011).
61. Belyy, V. et al. The mammalian dynein–dynactin complex is a strong opponent to kinesin in a tug-of-war competition. *Nat. Cell Biol.* **18**, 1018–1024 (2016).
62. Elshenawy, M. M. et al. Cargo adaptors regulate stepping and force generation of mammalian dynein–dynactin. *Nat. Chem. Biol.* **15**, 1093–1101 (2019).
63. Liu, X., Rao, L. & Gennerich, A. The regulatory function of the AAA4 ATPase domain of cytoplasmic dynein. *Nat. Commun.* **11**, 5952 (2020).
64. Pazour, G. J., Agrin, N., Leszyk, J. & Witman, G. B. Proteomic analysis of a eukaryotic cilium. *J. Cell Biol.* **170**, 103–113 (2005).
65. Witman, G. B. Isolation of *Chlamydomonas* flagella and flagellar axonemes. *Methods Enzymol.* **134**, 280–290 (1986).
66. Khataee, H. & Howard, J. Force generated by two kinesin motors depends on the load direction and intermolecular coupling. *Phys. Rev. Lett.* **122**, 188101 (2019).
67. Pyrpassopoulos, S., Shuman, H. & Ostap, E. M. Modulation of kinesin's load-bearing capacity by force geometry and the microtubule track. *Biophys. J.* **118**, 243–253 (2019).
68. Sedlak, S. M. et al. Monodisperse measurement of the biotin-streptavidin interaction strength in a well-defined pulling geometry. *PLoS ONE* **12**, e0188722 (2017).
69. Layden, H. M., Eleuteri, N. A., Hiebert, S. W. & Stengel, K. R. A protocol for rapid degradation of endogenous transcription factors in mammalian cells and identification of direct regulatory targets. *STAR Protoc.* **2**, 100530 (2021).
70. Redwine, W. B. et al. The human cytoplasmic dynein interactome reveals novel activators of motility. *eLife* **6**, e28257 (2017).
71. Reck-Peterson, S. L. et al. Single-molecule analysis of dynein processivity and stepping behavior. *Cell* **126**, 335–348 (2006).
72. Chaaban, S. & Carter, A. P. Structure of dynein–dynactin on microtubules shows tandem adaptor binding. *Nature* **610**, 212–216 (2023).
73. Lee, I. G., Cason, S. E., Alqassim, S. S., Holzbaur, E. L. F. & Dominguez, R. A tunable LIC1–adaptor interaction modulates dynein activity in a cargo-specific manner. *Nat. Commun.* **11**, 5695 (2020).
74. Reddy, B. J. et al. Load-induced enhancement of Dynein force production by LIS1–NudE in vivo and in vitro. *Nat. Commun.* **7**, 12259 (2016).

75. Nakata, T. & Hirokawa, N. Point mutation of adenosine triphosphate-binding motif generated rigor kinesin that selectively blocks anterograde lysosome membrane transport. *J. Cell Biol.* **131**, 1039–1053 (1995).
76. Zakeri, B. et al. Peptide tag forming a rapid covalent bond to a protein, through engineering a bacterial adhesin. *Proc. Natl Acad. Sci. USA* **109**, E690–E697 (2012).
77. Keeble, A. H. et al. Approaching infinite affinity through engineering of peptide–protein interaction. *Proc. Natl Acad. Sci. USA* **116**, 26523–26533 (2019).
78. Gennerich, A., Carter, A. P., Reck-Peterson, S. L. & Vale, R. D. Force-induced bidirectional stepping of cytoplasmic dynein. *Cell* **131**, 952–965 (2007).
79. Qiu, W. et al. Dynein achieves processive motion using both stochastic and coordinated stepping. *Nat. Struct. Mol. Biol.* **19**, 193–200 (2012).
80. DeWitt, M. A., Chang, A. Y., Combs, P. A. & Yildiz, A. Cytoplasmic dynein moves through uncoordinated stepping of the AAA+ ring domains. *Science* **335**, 221–225 (2012).
81. Mallik, R., Carter, B. C., Lex, S. A., King, S. J. & Gross, S. P. Cytoplasmic dynein functions as a gear in response to load. *Nature* **427**, 649–652 (2004).
82. Toba, S., Watanabe, T. M., Yamaguchi-Okimoto, L., Toyoshima, Y. Y. & Higuchi, H. Overlapping hand-over-hand mechanism of single molecular motility of cytoplasmic dynein. *Proc. Natl Acad. Sci. USA* **103**, 5741–5745 (2006).
83. Walter, W. J., Koonce, M. P., Brenner, B. & Steffen, W. Two independent switches regulate cytoplasmic dynein's processivity and directionality. *Proc. Natl Acad. Sci. USA* **109**, 5289–5293 (2012).
84. Rao, L., Berger, F., Nicholas, M. P. & Gennerich, A. Molecular mechanism of cytoplasmic dynein tension sensing. *Nat. Commun.* **10**, 3332 (2019).
85. Nicholas, M. P. et al. Cytoplasmic dynein regulates its attachment to microtubules via nucleotide state-switched mechanosensing at multiple AAA domains. *Proc. Natl Acad. Sci. USA* **112**, 6371–6376 (2015).
86. Hu, D. J.-K. et al. Dynein recruitment to nuclear pores activates apical nuclear migration and mitotic entry in brain progenitor cells. *Cell* **154**, 1300–1313 (2013).
87. Uemura, S. et al. Kinesin–microtubule binding depends on both nucleotide state and loading direction. *Proc. Natl Acad. Sci. USA* **99**, 5977–5981 (2002).
88. Budaitis, B. G. et al. Pathogenic mutations in the kinesin-3 motor KIF1A diminish force generation and movement through allosteric mechanisms. *J. Cell Biol.* **220**, e202004227 (2021).
89. Svoboda, K., Schmidt, C. F., Schnapp, B. J. & Block, S. M. Direct observation of kinesin stepping by optical trapping interferometry. *Nature* **365**, 721–727 (1993).
90. Svoboda, K. & Block, S. M. Force and velocity measured for single kinesin molecules. *Cell* **77**, 773–784 (1994).
91. Abid Ali, F. et al. KIF1C activates and extends dynein movement through the FHF cargo adapter. *Nat. Struct. Mol. Biol.* **32**, 756–766 (2025).
92. Siddiqui, N. et al. Force generation of KIF1C is impaired by pathogenic mutations. *Curr. Biol.* **32**, 3862–3870 (2022).
93. Gibson, J. M. et al. Coil-to-α-helix transition at the Nup358–BicD2 interface activates BicD2 for dynein recruitment. *eLife* **11**, e74714 (2022).
94. Cui, H. et al. Coiled-coil registry shifts in the F684I mutant of Bicaudal D result in cargo-independent activation of dynein motility. *Traffic* **21**, 463–478 (2020).
95. Noell, C. R. et al. Role of coiled-coil registry shifts in the activation of human Bicaudal D2 for dynein recruitment upon cargo binding. *J. Phys. Chem. Lett.* **10**, 4362–4367 (2019).
96. Terawaki, S., Yoshikane, A., Higuchi, Y. & Wakamatsu, K. Structural basis for cargo binding and autoinhibition of Bicaudal-D1 by a parallel coiled-coil with homotypic registry. *Biochem. Biophys. Res. Commun.* **460**, 451–456 (2015).
97. Liu, Y. et al. Bicaudal-D uses a parallel, homodimeric coiled coil with heterotypic registry to coordinate recruitment of cargos to dynein. *Genes Dev.* **27**, 1233–1246 (2013).
98. Lau, C. K. et al. Cryo-EM reveals the complex architecture of dynactin's shoulder region and pointed end. *EMBO J.* **40**, e106164 (2021).
99. Slivka, J. et al. Stepping dynamics of dynein characterized by MINFLUX. Preprint at *bioRxiv* https://doi.org/10.1101/2024.07.16.603667 (2024).
100. Zhang, R., LaFrance, B. & Nogales, E. Separating the effects of nucleotide and EB binding on microtubule structure. *Proc. Natl Acad. Sci. USA* **115**, E6191–E6200 (2018).
101. Nishida, N. et al. Structural basis for two-way communication between dynein and microtubules. *Nat. Commun.* **11**, 1038 (2020).
102. Mirdita, M. et al. ColabFold: making protein folding accessible to all. *Nat. Methods* **19**, 679–682 (2022).

Methods

DDB isolation from rat-brain lysate

To isolate brain dynein–dynactin–BicD2 complexes, frozen rat brains were homogenized in equal weight:volume of buffer (30 mM HEPES–KOH, 50 mM K-acetate, 1 mM EGTA and 5 mM $MgSO_4$, pH 7.2) using a Waring blender. The homogenate was centrifuged at 30,000*g* for 30 min. After clarification, the crude homogenate was flash-frozen in 2-ml aliquots for future use. The brain lysate aliquots were thawed rapidly and supplemented with 1 mM phenylmethylsulfonyl fluoride (PMSF), 5 mM dithiothreitol (DTT) and 0.1% NP-40, and the lysate was clarified further at 100,000*g* for 10 min before use. Purified BicD2N[22] (final concentration of 300 nM) was added to the samples, which were then incubated with Strep-tactin beads for 2 h at 4 °C. The beads were washed extensively with the same buffer. The bound complexes were eluted in assay buffer containing 3 mM desthiobiotin for 10 min on ice. The beads were removed by filtration through a 0.22-µm-pore spin filter. The complexes were used directly for optical-tweezers assays or flash-frozen in small aliquots after the addition of 10% sucrose as a cryoprotectant.

Plasmid and construct generation

The plasmids for human dynein complexes were provided by A. P. Carter (MRC Laboratory of Molecular Biology, Cambridge, UK). Plasmids for Lis1 constructs were gifts from S. Reck-Peterson (University of California, San Diego, USA). BicD2 constructs were generated by inserting a mouse BicD2(25–400) from a plasmid (Addgene, 64205)[103] into either a backbone for *E. coli* expression (pSNAP-tag(T7)-2 vector; New England Biolabs, N9181S)[88] or pET28b. Shorter BicD2 constructs were produced via Q5 mutagenesis (New England Biolabs, E0554S) and a single mutation (Y46D) was introduced into the BicD2(25–180) construct.

The kinesin-1 (KIF5B) (Cys-light) S43C construct[104] was provided by R. D. Vale (previously University of California, San Francisco, USA). To generate the rigor kinesin construct, a single mutation (T92N) was introduced and a SpyTag003 was inserted at the C terminus using Q5 mutagenesis. The SpyCatcher003 tag, amplified from the SpyCatcher003-S49C plasmid[77] (Addgene, 133448), was inserted to the C terminus of BicD2. Plasmids for Tev protease[105] (Addgene, 171782) and BirA (Addgene, 20857)[106] were obtained from Addgene.

All plasmids generated for this study were validated through Sanger sequencing (Genomics Core Facility, Albert Einstein College of Medicine) or full-plasmid sequencing (Azenta). The constructs used in this study are listed in Supplementary Table 1.

Tagging dynactin in HEK293T/17 SF cells using CRISPR

A HaloTag-3×FLAG-P2A-mCherry tag was inserted at the C terminus of the DCTN4 (p62) subunit of dynactin using a CRISPR-based method adapted from a previously published protocol[69]. The HaloTag-3×FLAG has been used successfully in a stable adherent HEK293T cell line for dynactin purification[57]. The *DCTN4* gene and 1 kb downstream sequence were retrieved from the UCSC Genome Browser (https://genome.ucsc.edu/; Ensembl ID (ENSG00000132912)) and the guide RNA was designed using the CRISPOR online tool (https://crispor.gi.ucsc.edu/)[107]. The guide RNA (5′-TCCTTAAAAGG TTCCACTGG-3′) was ordered as Alt-R CRISPR RNA (crRNA) from IDTDNA, along with Alt-R *trans*-activating crRNA (IDTDNA, 1072532) and Alt-R Cas9 nuclease (IDTDNA, 1081058). These RNAs were dissolved in nuclease-free duplex buffer (IDTDNA) to a final concentration of 100 µM.

To construct the targeting plasmid, 303 base pairs upstream of the *DCTN4* stop codon were amplified from HEK293T/17 SF genomic DNA and stitched with HaloTag-P2A-mCherry, followed by 611 base pairs of downstream *DCTN4* sequences. The resulting DNA fragment was then inserted into a backbone plasmid and the construct was confirmed by full-plasmid sequencing (Azenta).

Cell culture and preparation

One millilitre of HEK293T/17 SF cells (ATCC, ACS-4500) was recovered following the vendor's instructions in 10 ml complete medium (9.8 ml of BalanCD HEK293 (Fujifilm Irvine Scientific, 91165-1L), 0.1 ml of 100×GlutaMAX supplement (Gibco, 35050061), 0.1 ml of 100×insulin–transferrin–selenium (Corning, 25-800-CR) and 20 µl anti-clumping agent (Gibco, 0010057DG)). The cultures were incubated at 37 °C, with 5% CO_2 (Eppendorf, New Brunswick S41i CO2 Incubator Shaker) and shaking at 125 rpm, and maintained at a density of $<2 \times 10^6$ cells ml^{-1}.

Electroporation and CRISPR delivery

For CRISPR delivery, 3 µl crRNA, 3 µl *trans*-activating crRNA and 4 µl Neon NxT resuspension R buffer (ThermoFisher, NEON1S) were mixed, annealed (incubated at 95 °C for 5 min) and then cooled to room temperature (RT). Cas9 protein (1.5 µl of the 10 mg ml^{-1}) was added to the RNA mixture and incubated at RT for 15 min, followed by the addition of 6 µg of the targeting plasmid.

HEK293T/17 SF cells (5×10^6) were pelleted at 140*g* for 5 min, washed with 10 ml PBS and then resuspended in 100 µl Neon NxT R Buffer. The prepared Cas9–RNA–plasmid complex was mixed with the resuspended cells and electroporated at 1,100 V for 20 ms with two pulses using the Neon NxT Electroporation System (ThermoFisher, NEON1S) as per the manufacturer's instruction. The electroporated cells were immediately transferred to 2 ml complete medium in a six-well plate and allowed to recover for two days at 37 °C without shaking. Following recovery, approximately 1×10^7 cells were sorted using a BD Aria cell sorter to select for mCherry-positive cells. The sorted cells were then cultured, frozen and stored in liquid nitrogen for future use.

Dynactin purification

HEK293T/17 SF cells expressing p62 tagged with HaloTag-3×FLAG were cultured in 800 ml medium at a density of 2×10^6 cells ml^{-1} and harvested by centrifugation at 600*g* for 10 min at 4 °C. The resulting pellet (approximately 10 ml) was resuspended in 10 ml of 2×dynactin lysis buffer containing 60 mM HEPES (pH 7.2), 200 mM NaCl, 4 mM $MgCl_2$, 2 mM EGTA, 20% glycerol, 0.2 mM ATP, 2 mM DTT, 0.4% (vol/vol) Triton X-100 and two EDTA-free protease inhibitor cocktail tablets (Roche, 11836170001). The suspension was nutated at 4 °C for 15 min. The lysate was then cleared by centrifugation at 80,000 rpm (260,000*g*, *k*-factor = 28) for 10 min using a TLA-110 rotor in a Beckman Tabletop Optima TLX ultracentrifuge.

Anti-FLAG M2 affinity gel (1 ml; Sigma, A2220) was washed with 5 ml of 1×dynactin lysis buffer. The cleared lysate was added to the resin and nutated overnight at 4 °C. The resin was subsequently washed with 40 ml wash buffer containing 30 mM HEPES (pH 7.2), 250 mM KCl, 2 mM $MgCl_2$, 1 mM EGTA, 10% glycerol, 0.1 mM ATP, 1 mM DTT, 0.2% (wt/vol) Pluronic F-127 and 0.5 mM Pefabloc. The resin was then transferred to a 2-ml tube and incubated with 200 µl wash buffer containing 100 µl of 5 mg ml^{-1} FLAG peptide. This mixture was nutated at 4 °C for 30 min. The supernatant containing the purified dynactin was collected and concentrated using an Amicon Ultra-0.5 ml centrifugal filter unit (100-kDa molecular weight cutoff) at 5,000*g* and 4 °C. A Bradford assay (ThermoFisher, 23200) was used to determine the dynactin concentration. The subunit composition of dynactin was confirmed by mass spectrometry.

Dynactin from porcine brain

Porcine-brain dynactin[23] was provided by A. P. Carter (MRC Laboratory of Molecular Biology, Cambridge, UK).

Sf9 expression of cytoplasmic dynein-1 and Lis1

The full cytoplasmic dynein-1 complex, the tail complex, the phi-mutant complex and Lis1 were expressed in Sf9 cells following established protocols[23,57]. Briefly, a bacmid was generated by transforming the plasmid containing the desired construct into MAX efficiency DH10Bac

competent cells (Gibco, 10361012). Recombinant bacmid insertion was verified by blue–white screening and confirmed by PCR.

One millilitre of Sf9 cells cultured in Sf-900 II SFM (ThermoFisher, 11496015) was recovered and cultured in 10 ml Sf-900 II SFM medium (ThermoFisher, 10902104) at 27 °C with shaking at 135 rpm. The cultures were maintained at a density of $<2 \times 10^6$ cells ml^{-1}. For transfection, 2 ml of a 0.5×10^6 cells ml^{-1} culture was seeded in a six-well plate. A mixture of 2 µg bacmid and 200 µl medium was prepared, to which 6 µl FuGENE HD transfection reagent (Promega, E2311) was added.

After incubation at RT for 15 min, the mixture was added dropwise to the cells. The culture was then incubated at 27 °C without shaking for four days to generate P1 virus. The P1 virus was collected, transferred to a 15-ml tube and stored at 4 °C in the dark. To produce P2 virus, 0.5 ml P1 virus was added to 50 ml culture (1.5×10^6 cells ml^{-1}) and incubated at 27 °C with shaking at 135 rpm for three days. The P2 virus was harvested by centrifugation at 2,000*g* and 4 °C for 10 min and stored at 4 °C in the dark. For protein expression, 5 ml P2 virus was added to 500 ml culture of Sf9 cells at a density of 2×10^6 cells ml^{-1}. The culture was incubated at 27 °C with shaking (135 rpm) for 60–72 h. The cells were harvested by centrifugation at 2,000*g* and 4 °C for 15 min. The pellet was washed with 40 ml cold PBS and centrifuged again at 2,000*g* and 4 °C for 10 min. The supernatant was discarded; the pellet was flash-frozen in liquid nitrogen and stored at −80 °C until further use.

Cytoplasmic dynein-1 and Lis1 purification

The cell pellet (approximately 5 ml) was resuspended in 5 ml of 2×lysis buffer containing 60 mM HEPES (pH 7.2), 300 mM KCl, 4 mM $MgCl_2$, 2 mM EGTA, 20% (vol/vol) glycerol, 0.4 mM ATP, 4 mM DTT, 0.2% (wt/vol) Pluronic F-127, 100 µl of 2.5 U µl^{-1} DNase I and two EDTA-free protease inhibitor cocktail tablets. The resuspended pellet was dounced for 30 strokes on ice. The lysate was cleared by centrifugation as described for dynactin purification. Four millilitres of IgG Sepharose 6 Fast Flow affinity resin (Cytiva, 17096901) was pre-washed with 6 ml lysis buffer. The cleared lysate was added to the resin and nutated at 4 °C for 4 h. The resin was then washed with 50 ml wash buffer containing 50 mM HEPES (pH 7.2), 150 mM KCl, 2 mM $MgCl_2$, 1 mM EGTA, 10% (vol/vol) glycerol, 0.1 mM ATP, 1 mM DTT, 0.1% (wt/vol) Pluronic F-127 and 1 mM PMSF.

To label the SNAP tag on the N terminus of the dynein heavy chain, 15 µl of 1 mM SNAP-tag dye was added to the resin and the mixture was nutated at 4 °C overnight. The resin was then washed with 50 ml TEV-release buffer containing 50 mM HEPES (pH 7.2), 150 mM KCl, 2 mM $MgCl_2$, 1 mM EGTA, 10% (vol/vol) glycerol, 0.1 mM ATP, 1 mM DTT and 0.1% (wt/vol) Pluronic F-127. The resin was subsequently transferred to a 5-ml tube with TEV-release buffer to a final volume of 5 ml. Fifty microlitres of 200 µM MBP-superTev protease was added to the resin and the mixture was nutated overnight at 4 °C in the dark. One millilitre of amylose resin (New England Biolabs, E8021S) was used to remove the MBP-superTev protease. The supernatant was concentrated following the same protocol used for dynactin purification. The purity of the cytoplasmic dynein-1 complex and Lis1 was verified by 4–12% *bis*-Tris polyacrylamide gel electrophoresis and its concentration was determined using the Bradford assay.

E. coli-based expression

BicD2 constructs were expressed in *E. coli*. Each plasmid was transformed into BL21-CodonPlus(DE3)-RIPL competent cells (Agilent Technologies, 230280), and a single colony was picked and inoculated in 1 ml terrific broth containing 50 µg ml^{-1} carbenicillin and 50 µg ml^{-1} chloramphenicol. The 1-ml culture was incubated at 37 °C overnight with shaking and subsequently inoculated into 400 ml terrific broth supplemented with 2 µg ml^{-1} carbenicillin and 2 µg ml^{-1} chloramphenicol. The culture was incubated at 37 °C with shaking for 5 h and cooled to 16 °C for 1 h. Protein expression was induced with 0.1 mM isopropyl β-D-1-thiogalactopyranoside (overnight at 16 °C). The cells were harvested by centrifugation at 3,000*g* and 4 °C for 10 min, and the supernatant was discarded. The cell pellet was resuspended in 5 ml B-PER complete bacterial protein extraction reagent (ThermoFisher Scientific, 89821) supplemented with 2 mM $MgCl_2$, 1 mM EGTA, 1 mM DTT, 0.1 mM ATP and 2 mM PMSF. The resuspension was flash-frozen in liquid nitrogen and stored at −80 °C.

Purification of *E. coli*-expressed constructs

To purify *E. coli*-expressed protein, the frozen cell pellet was thawed at 37 °C and nutated at RT for 20 min to lyse the cells. The cell lysate was cleared as for dynactin purification. The supernatant was passed through 500 µl Ni-NTA Roche cOmplete His-Tag purification resin (Millipore Sigma, 5893682001) for His-tagged proteins or Strep-Tactin 4Flow high-capacity resin (IBA Lifesciences GmbH, 2-1250-010) for strep-II-tagged proteins. The resin was washed with 10 ml wash buffer containing 50 mM HEPES (pH 7.2), 300 mM KCl, 2 mM $MgCl_2$, 1 mM EGTA, 1 mM DTT, 1 mM PMSF, 0.1 mM ATP, 0.1% (wt/vol) Pluronic F-127 and 10% glycerol. The proteins were eluted with elution buffer (50 mM HEPES, pH 7.2, 150 mM KCl, 2 mM $MgCl_2$, 1 mM EGTA, 1 mM DTT, 1 mM PMSF, 0.1 mM ATP, 0.1% Pluronic F-127 (wt/vol) and 10% glycerol) supplemented with either 150 mM imidazole for His-tagged proteins or 5 mM desthiobiotin for strep-II-tagged proteins. The eluate was either flash-frozen and stored at −80 °C or concentrated using an Amicon Ultra-0.5 ml centrifugal filter unit (30-kDa molecular weight cutoff; Sigma, UFC503024) before flash-freezing. The purity and concentration of the proteins were analysed using 4–12% *bis*-Tris polyacrylamide gels. For biotinylation of BicD2, 50 µl of 10 µM BicD2 was mixed with 1 µl of 100 mM ATP, 2 µl of 50 µM BirA and 1 µl of 10 mM biotin, followed by incubation at 30 °C for 2 h. The BirA was subsequently removed using Ni-NTA resin and the solution was buffer-exchanged into 30 mM HEPES (pH 7.2), 50 mM KCl, 2 mM $MgCl_2$, 1 mM EGTA, 1 mM DTT, 0.1% (wt/vol) Pluronic F-127 and 10% glycerol to remove free biotin.

Purification of the BicD2–rigor kinesin constructs

The purification of BicD2–rigor kinesin constructs followed the same protocol as for *E. coli*-expressed constructs, with modifications to facilitate complex formation. After the cells were thawed, the BicD2 and kinesin solutions were combined and nutated at RT for 20 min, followed by additional nutation at 4 °C for 2 h to allow binding between SpyCatcher003 and SpyTag003. The lysate was then passed through Ni-NTA resin to capture His-tagged components. The elution from the Ni-NTA resin was subsequently passed through Strep-Tactin resin to isolate the fully formed BicD2–kinesin complex. The final eluate from the Strep-Tactin resin was further concentrated following the protocol used for dynactin purification.

Mass photometry

For DDB purified from rat-brain lysate, chambers were prepared by cleaning high-precision microscope coverslips (number 1.5, 24 × 50; Marienfeld Superior, 0107222,) by sequential sonication in ultrapure H_2O (10 min), isopropanol (10 min) and ultrapure H_2O, followed by drying with filtered air. Culturewell gaskets (3 mm diameter × 1 mm depth; Grace Bio-Labs, 103250) were cut, rinsed with isopropanol and ultrapure H_2O, dried with filtered air, and placed onto the freshly cleaned coverslips. The protein samples were diluted in SRP90 buffer (90 mM HEPES–KOH, 50 mM K-acetate, 2 mM Mg-acetate, 1 mM EGTA and 10% glycerol) immediately before data acquisition. Data were acquired on a OneMP mass photometer (Refeyn Ltd) at 1 kHz for 60 s using AcquireMP (Refeyn Ltd). Each sample was measured at least three times. A MassFerence P1 calibrant (Refeyn, MP-CON-41033) was used for calibration, and data analysis was performed with DiscoverMP (Refeyn Ltd). To verify the stoichiometry and molecular weight of BicD–rigor kinesin complexes, we used the MassGlass UC sample prep kit (Refeyn, MP-CON-21022) and acquired data on a TwoMP mass photometer (Refeyn), with the sample diluted in PBS buffer.

Optical-tweezers assay

Polystyrene beads. Anti-GFP polystyrene beads were prepared by covalently binding anti-GFP and BSA to carboxyl polystyrene beads (0.52 µm; Polysciences, 09836-15) using NHS-EDAC chemistry[84]. Streptavidin beads (0.55 µm) were purchased from Spherotech (SVP-05-10).

Microtubule polymerization. Two microlitres of 10 mg ml^{-1} tubulin (Cytoskeleton, T240-B) were mixed with 2 µl of 1 mg ml^{-1} biotinylated tubulin (Cytoskeleton, T333P-A) and 1 µl of 10 mM GTP. The mixture was incubated at 37 °C for 20 min. After incubation, 0.5 µl of 0.2 mM paclitaxel in dimethylsulfoxide was added, and the incubation was continued for an additional 20 min. The solution was carefully layered on top of a 100 µl glycerol cushion (80 mM PIPES, pH 6.8, 2 mM $MgCl_2$, 1 mM EGTA, 60% (vol/vol) glycerol, 1 mM DTT and 10 µM paclitaxel) in a 230-µl TLA100 tube (Beckman Coulter, 343775) and centrifuged at 80,000 rpm (250,000*g*, *k*-factor = 10) for 5 min at RT. The supernatant was gently removed and the pellet was resuspended in 11 µl BRB80G10 (80 mM PIPES, pH 6.8, 2 mM $MgCl_2$, 1 mM EGTA, 10% (vol/vol) glycerol, 1 mM DTT and 10 µM paclitaxel). The microtubule solution was stored at RT in the dark for further use.

Flow chamber preparation. A flow chamber was assembled using a glass slide (Fisher Scientific, 12-550-123) and an ethanol-cleaned coverslip (Zeiss, 474030-9000-000), separated by two thin strips of parafilm. Ten microlitres of 0.5 mg ml^{-1} BSA–biotin (ThermoScientific, 29130) were introduced into the chamber and incubated for 10 min. The chamber was then washed with 2 × 20 µl blocking buffer (80 mM PIPES, pH 6.8, 2 mM $MgCl_2$, 1 mM EGTA, 10 µM paclitaxel, 1% (wt/vol) Pluronic F-127, 2 mg ml^{-1} BSA and 1 mg ml^{-1} α-casein) and incubated for 30 min to block the surface. Next, 10 µl of 0.25 mg ml^{-1} streptavidin (Promega, Z7041) was introduced into the chamber and incubated for 10 min. The chamber was washed with 2 × 20 µl blocking buffer, followed by the addition of 10 µl of 0.02 mg ml^{-1} biotin-labelled microtubules in the blocking buffer, which were incubated for 1 min. After another wash with 2 × 20 µl blocking buffer, the chamber was stored in a humidity chamber until further use.

Sample preparation. Dynein (dimer), dynactin and BicD2 (dimer) were mixed in a 1:1:1 ratio to a final concentration of 200 nM each. The solution was incubated overnight at 4 °C to allow complex formation. One microlitre of polystyrene trapping beads was mixed with 1 µl motility buffer (60 mM HEPES, pH 7.2, 50 mM KCl, 2 mM $MgCl_2$, 1 mM EGTA, 10 µM paclitaxel, 0.5% (wt/vol) Pluronic F-127, 5 mg ml^{-1} BSA and 0.2 mg ml^{-1} α-casein) and 1 µl of appropriately diluted DDB complex. The mixture was incubated on ice for 30 min. Following incubation, 40 µl motility buffer supplemented with 2 mM ATP, 2 mM biotin and a gloxy oxygen scavenger system was added to the bead–protein solution. Two 20-µl volumes of the solution were then introduced into the chamber. The chamber was sealed with vacuum grease to prevent evaporation.

Data acquisition. Optical tweezers experiments were performed using a C-Trap combined with TIRF and interference reflection microscopy (C-Trap Edge, LUMICKS) at RT. Microtubules were visualized using interference reflection microscopy. The trap stiffness was adjusted to 0.08–0.10 pN nm^{-1}. Optical-trapping data were sampled at a rate of 20 MHz and digitally downsampled by a factor of 256, resulting in a final sample rate of 78.125 kHz. An anti-aliasing filter was applied to achieve a passband of 31.25 kHz. The resulting data were fitted to a Lorentzian power spectrum for analysis.

Data analysis. Optical trapping data were processed using a custom MATLAB program. A built-in MATLAB step-finding algorithm was applied to traces that were downsampled by a factor of 80 through averaging. Steps with forces of <0.2 pN were excluded. For each step, the combined stiffness of the motor and bead-linkage, $k_{\text{m-link}}$, was calculated using the original data[108], where k_B is the Boltzmann constant, σ^2 is the variance (which depends on the bead position x_b), T is the temperature and k_{trap} is the trap stiffness, as follows:

$$k_{\text{m-link}} = \frac{k_B T}{\sigma^2(x_b)} - k_{\text{trap}}.$$

Steps for each trace were binned into 0.5-pN force windows. The mean value of the 25th to 75th percentiles for each force window (for example, dwell time, step sizes and velocity) were calculated to represent in the force window. Traces with similar forces were grouped, and the mean and s.e.m. were calculated and visualized using Prism 10 (GraphPad). To compensate for the linkage compliance, the difference between the motor stretch (F / $k_{\text{m-link}}$) for each force window in each group was calculated and added to the steps.

To statistically compare the fractions of different stall events shown in Figs. 2c and 3a, we used a two-proportion Z-test.

Total internal reflection fluorescence assay

Sample preparation and triple-dynein and dual-adaptor co-localization. Microtubule polymerization and flow chamber preparation were performed as described for the optical-tweezers assay. After microtubules were immobilized on the coverslip surface, the assembled complex was diluted in the motility buffer containing 60 mM HEPES (pH 7.2), 75 mM KCl, 2 mM $MgCl_2$, 1 mM EGTA, 1 mM DTT, 2 mM ATP, 0.5% Pluronic F-127 (wt/vol) and 10% glycerol. The solution was introduced into the slide chamber, which was then sealed with vacuum grease to prevent evaporation.

For three-colour co-localization TIRF experiments, DDB complexes containing either BicD2(400)–rigor kinesin or BicD2(400) alone were pre-assembled overnight in a 3:1:1 dynein:dynactin:BicD2 ratio in motility buffer supplemented with 100 µM ATPγS. The three dyneins were differently labelled with Alexa Fluor 647, TMR and Alexa Fluor 488. After constructing the flow chamber and immobilizing microtubules, 10 nM of either BicD2(25–180) or BicD2(25–180, Y46D) was added to the pre-assembled complexes and introduced into the chamber. For Lis1-containing assays, 20 nM Lis1 was included. In all cases, the final motility buffer contained 100 µM ATPγS in place of 2 mM ATP.

For the dual-adaptor co-localization assay, DDB complexes containing CF488-labelled BicD2(25–400)–rigor kinesin and unlabelled dynein were pre-assembled overnight at a 3:1:1 dynein:dynactin:BicD2 molar ratio. After constructing the flow chamber and immobilizing microtubules, 10 nM TMR-labelled BicD2(25–180) was added to the pre-assembled complexes and introduced into the chamber together with 100 µM ATPγS. Across nine independent flow-cell experiments (three technical replicates), we observed a total of 15 co-localization events. On average, each field of view (81.9 × 81.9 µm, 5-min recordings) contained approximately 250 CF488-labelled molecules, reflecting the number of rigor kinesin species bound to microtubules irrespective of their incorporation into DDB complexes. The detection of only 1–2 moving DDB–rigor kinesin complexes bound to the accessory adaptor per field of view therefore represents a substantial underestimation of the true number of co-localization events, owing to several technical limitations.

First, the efficiency of forming microtubule-bound DDB–rigor kinesin complexes containing two BicD2 molecules and three dyneins—which involves an assembly process that depends on force—is unknown, as the degree of tension developed in these complexes could not be quantified. DDB complexes containing one or two dyneins probably remain stationary as they generate only approximately 4.5 and 7 pN of force, respectively, whereas detachment of the microtubule-bound rigor kinesin (required for forward movement) probably requires forces of >7 pN (ref. 87). Second, the incorporation efficiency of

CF488-labelled BicD2–rigor kinesin into DDB complexes is unlikely to be complete. Uncoupled CF488–BicD2–rigor kinesin molecules can still bind microtubules but do not contribute to detectable moving dual-adaptor assemblies, further lowering the observed frequency. Third, the CF488 dye used to label the rigor kinesin–BicD2(25–400) is prone to photobleaching under TIRF illumination, often resulting in signal loss before movement becomes apparent due to the slow stepping velocity of these complexes (Extended Data Fig. 4). Finally, visualization of moving complexes bound to TMR–BicD2(25–180) requires concentrations of at least 10 nM, which generate substantial background fluorescence that obscures single-molecule detection across most of the field of view. Single TMR-labelled BicD2 molecules could only be resolved in peripheral regions where the excitation intensity was sufficiently low, which explains why co-localizations were detected almost exclusively in these areas. Together, these factors markedly reduce the probability of observing simultaneous co-localization events, indicating that the measured frequency represents a conservative estimate of the true occurrence of two-adaptor assemblies.

Data acquisition. Images were acquired using the BioVis software (BioVision Technologies) with an acquisition time of either 200 ms or 1,000 ms per frame.

Data analysis. Kymographs were generated using Fiji[109] and velocities were analysed using a custom MATLAB program.

AlphaFold2 structure prediction

The interaction between mouse BicD2(25–180) and human LIC2(417–444) was predicted using ColabFold (v1.5.5: AlphaFold2 using MMseqs2)[102].

Graphic visualization

Molecular structures in the figures were visualized using UCSF ChimeraX[110].

Statistics and reproducibility

No statistical method was used to pre-determine sample size and no data were excluded from the analyses. The experiments were not randomized and investigators were not blinded to allocation during experiments or outcome assessment. Data distributions were assumed to be normal for the purposes of statistical testing, although this was not formally tested.

Reporting summary

Further information on research design is available in the Nature Portfolio Reporting Summary linked to this article.

Data availability

Data supporting the findings of this manuscript are available from the corresponding author on reasonable request. Structural datasets re-analysed in this work include the PDB entries 6DPV, 6KIQ, 6PSE and 7Z8F. Gene and sequence information used for construct design include the DCTN4 gene (Ensembl accession ENSG00000132912). Source data are provided with this paper.

References

103. Bentley, M., Decker, H., Luisi, J. & Banker, G. A novel assay reveals preferential binding between Rabs, kinesins, and specific endosomal subpopulations. *J. Cell Biol.* **208**, 273–281 (2015).
104. Yildiz, A., Tomishige, M., Vale, R. D. & Selvin, P. R. Kinesin walks hand-over-hand. *Science* **303**, 676–678 (2004).
105. Keeble, A. H. et al. DogCatcher allows loop-friendly protein–protein ligation. *Cell Chem. Biol.* **29**, 339–350 (2022).
106. Howarth, M., Takao, K., Hayashi, Y. & Ting, A. Y. Targeting quantum dots to surface proteins in living cells with biotin ligase. *Proc. Natl Acad. Sci. USA* **102**, 7583–7588 (2005).
107. Concordet, J. P. & Haeussler, M. CRISPOR: intuitive guide selection for CRISPR/Cas9 genome editing experiments and screens. *Nucleic Acids Res.* **46**, W242–W245 (2018).
108. Liu, X., Rao, L., Qiu, W., Berger, F. & Gennerich, A. Kinesin-14 HSET and KlpA are non-processive microtubule motors with load-dependent power strokes. *Nat. Commun.* **15**, 6564 (2024).
109. Schindelin, J. et al. Fiji: an open-source platform for biological-image analysis. *Nat. Methods* **9**, 676–682 (2012).
110. Meng, E. C. et al. UCSF ChimeraX: tools for structure building and analysis. *Protein Sci.* **32**, e4792 (2023).

Acknowledgements

We thank the Albert Einstein College of Medicine Flow Cytometry Core Facility (Einstein National Cancer Institute's Cancer Center support grant P30CA013330), especially M. Liu, for assistance with sorting HEK293T cells. We also thank J. O. Wirth (Abberior) for valuable discussions on step-finding algorithms. L.R., X.L. and A.G. were supported by National Institutes of Health (NIH) grants R01GM098469 and acknowledge the use of LUMICKS C-Trap, funded by the NIH grant S10OD034445-01. R.J.M. and K.O. were supported by NIGMS National Institutes of Health grant GM124889. M.A. and K.S. were supported by National Institutes of Health grant R35GM147213. S.S. acknowledges the funding from the Hevolution Foundation (AFAR), the Einstein–Mount Sinai Diabetes Center and the NIH Office of the Director (grant number S10OD030286). Molecular graphics and analyses performed with UCSF ChimeraX, developed at the University of California, San Francisco, with support from NIH R01-GM129325 and the Office of Cyber Infrastructure and Computational Biology, National Institute of Allergy and Infectious Diseases.

Author contributions

L.R. produced and purified proteins, and designed the research together with A.G. L.R. and X.L. expressed and purified proteins. L.R., F.B. and A.G. analysed the data. L.R. and A.G. wrote the manuscript. A.G. secured funding. R.J.M. generated and provided proteins purified from rat-brain lysate for the initial studies[22]. K.O. performed and analysed mass photometry measurements of DDB motor complexes purified from rat brain. M.A. and K.S. assisted with CRISPR-based dynactin construct generation. S.S. performed mass spectrometry analysis of dynactin.

Competing interests

The authors declare no competing interests.

Additional information

Extended data is available for this paper at https://doi.org/10.1038/s41556-026-01877-0.

Supplementary information The online version contains supplementary material available at https://doi.org/10.1038/s41556-026-01877-0.

Correspondence and requests for materials should be addressed to Lu Rao or Arne Gennerich.

Peer review information *Nature Cell Biology* thanks William Hancock and the other, anonymous, reviewer(s) for their contribution to the peer review of this work. Peer reviewer reports are available.

https://doi.org/10.1038/s41556-026-01877-0

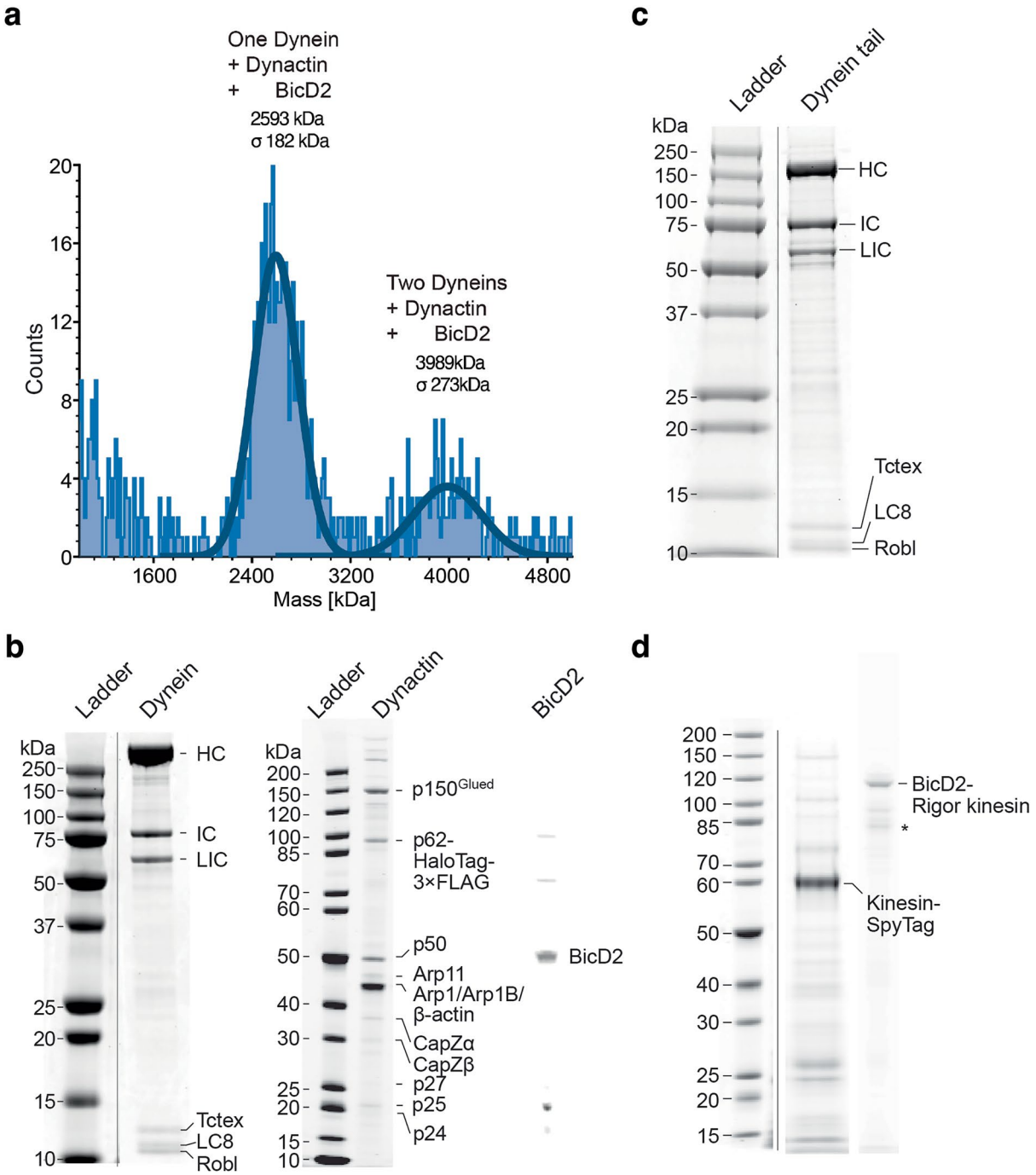

Extended Data Fig. 1 | Mass photometry of dynein–dynactin–BicD2 complexes purified from rat-brain lysate and polyacrylamide gels of purified proteins. **a**, Mass photometry reveals a ~2.6-MDa species corresponding to one-dynein DDB complexes and a ~4 MDa, corresponding to two-dynein DDB complexes. **b**, Polyacrylamide gels of human dynein complexes, dynactin complexes, and BicD2(25–400). Protein bands were assigned by molecular weight; dynactin subunits were further confirmed by mass spectrometry. **c**, Purified human dynein tail complexes (HC(1–1455)), which lack the heavy-chain motor domain. Associated subunits (IC, LIC, and light chains Tctex, LC8, and Robl) are present. **d**, Purified kinesin-SpyTag and BicD2–rigor kinesin. *Indicates minor truncated side products.

https://doi.org/10.1038/s41556-026-01877-0

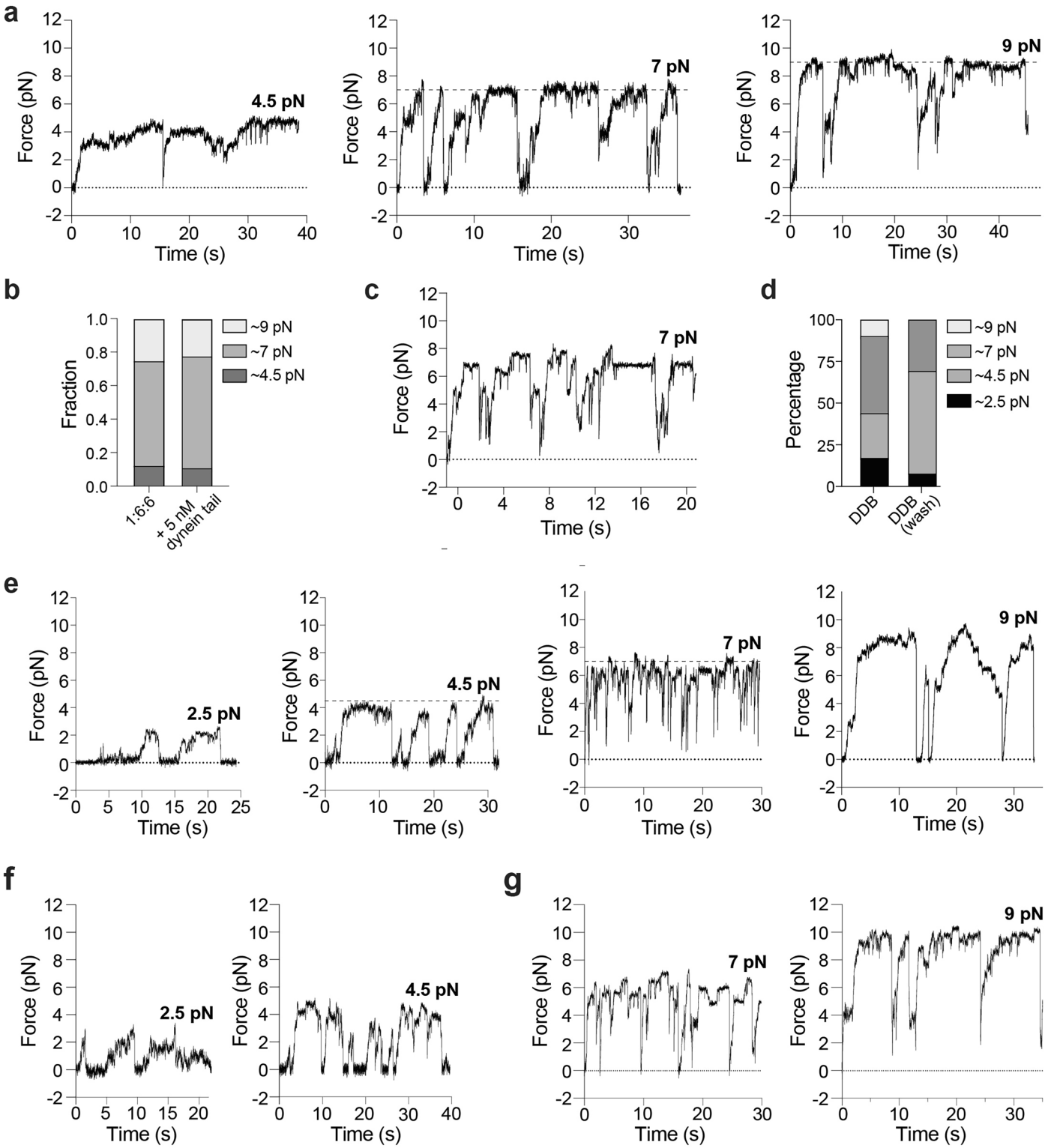

Extended Data Fig. 2 | Force generation of D^{act}DB complexes and DDB(276), DDB(180) and DDB(400) variants, and effects of dynein tail, free dynein and BicD2. a, Example traces of D^{act}DB stalling at ~4.5, ~7 and ~9 pN (downsampled 400-fold for visualization). **b**, Fractions of beads generating forces corresponding to D_1DB (fully activated), D_2DB, and D_3DB. For 1:6:6 (dynein^{act}:dynactin:BicD), the distributions were 12%, 62%, 26% (n = 9); with +5 nM dynein tail, 11%, 67%, 22% (n = 8). **c**, Representative trace of a DDB complex stalling at ~7 pN in the presence of 5 nM free dynein (downsampled 400-fold). **d**, Fraction of beads showing different force-generation behaviours with or without a wash step. Beads were incubated with DDB complexes and either assayed directly (DDB) or gently washed to remove free dynein before measurement (DDB (wash)). Stall-force distributions: DDB, 17%, 27%, 46%, 10% (n = 41); DDB (wash), 8%, 61%, 31%, 0% (n = 13). **e**, Example traces of DDB(276) stalling at ~2.5, ~4.5, ~7 pN, and ~9 pN (downsampled 400-fold). **f**, Example traces of DDB(180) generating ~2.5 and ~4.5 pN forces (downsampled 400-fold). **g**, Example traces showing DDB(400) stalling at 6–7 pN and 9–10 pN in the presence of 5 nM dynein and 5 nM BicD2(25–180) (downsampled 400-fold).

https://doi.org/10.1038/s41556-026-01877-0

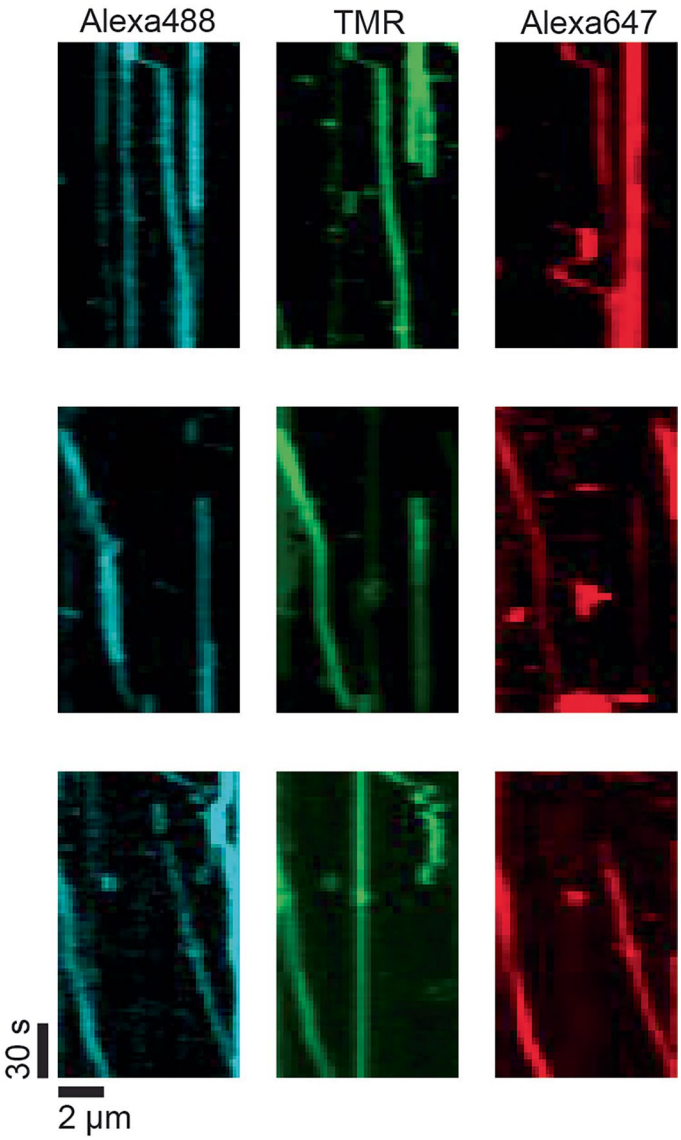

Extended Data Fig. 3 | Representative kymographs of DDB–rigor kinesin complexes containing three differently labelled dyneins. Representative kymographs of DDB–rigor kinesin complexes containing three differently labelled dyneins (Alexa Fluor 488, TMR, and Alexa Fluor 647) moving along surface-immobilized microtubules in the presence of 100 µM ATPγS.

https://doi.org/10.1038/s41556-026-01877-0

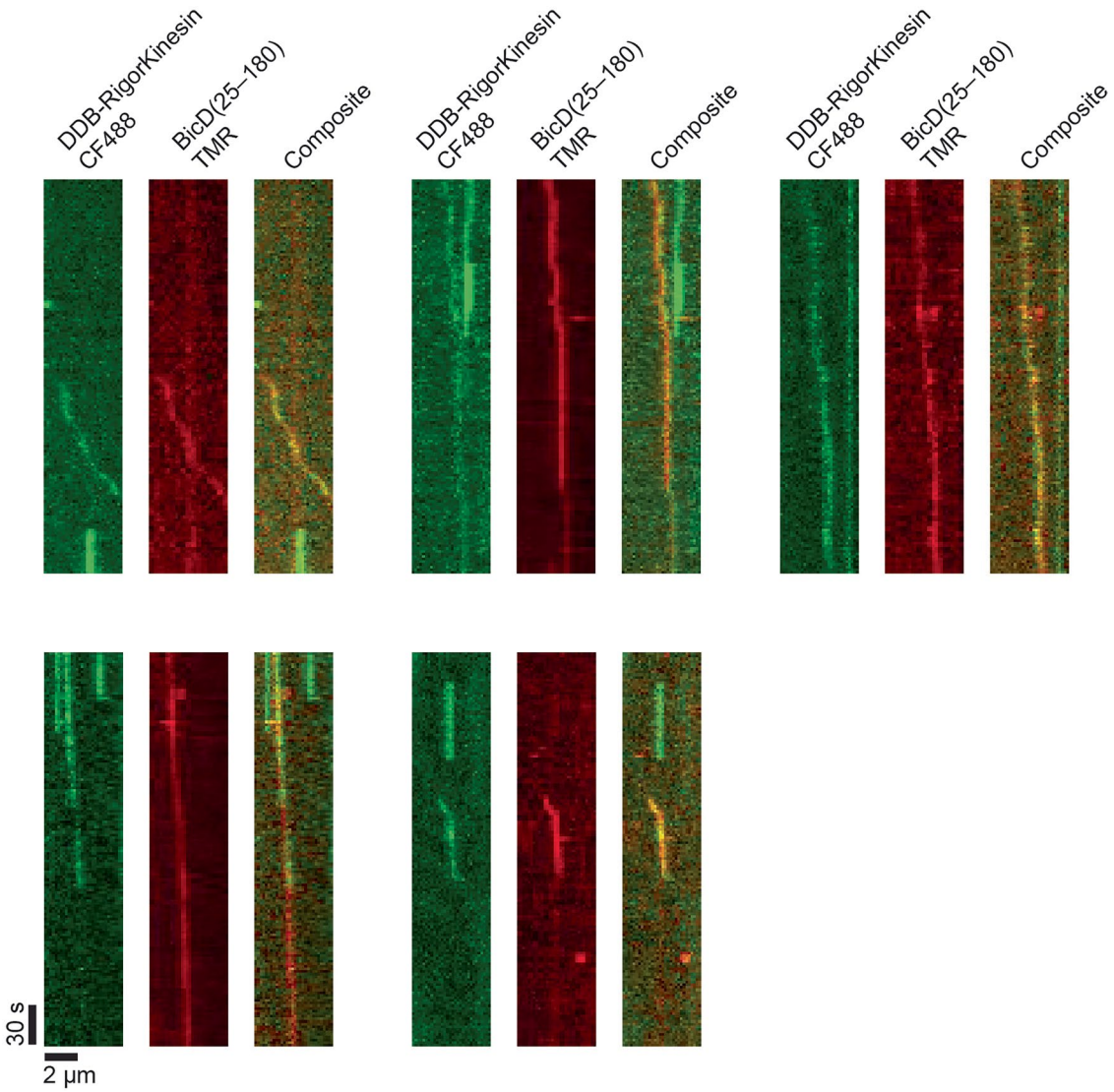

Extended Data Fig. 4 | Co-localization of an auxiliary BicD2(25–180) and a rigor kinesin–BicD2(25–400) complex. Example traces showing co-localization of TMR-labelled BicD2(25–180) and CF488-labelled rigor kinesin conjugated to BicD2(25–400) moving slowly along a surface-bound microtubule in the presence of 100 µM ATPγS.

https://doi.org/10.1038/s41556-026-01877-0

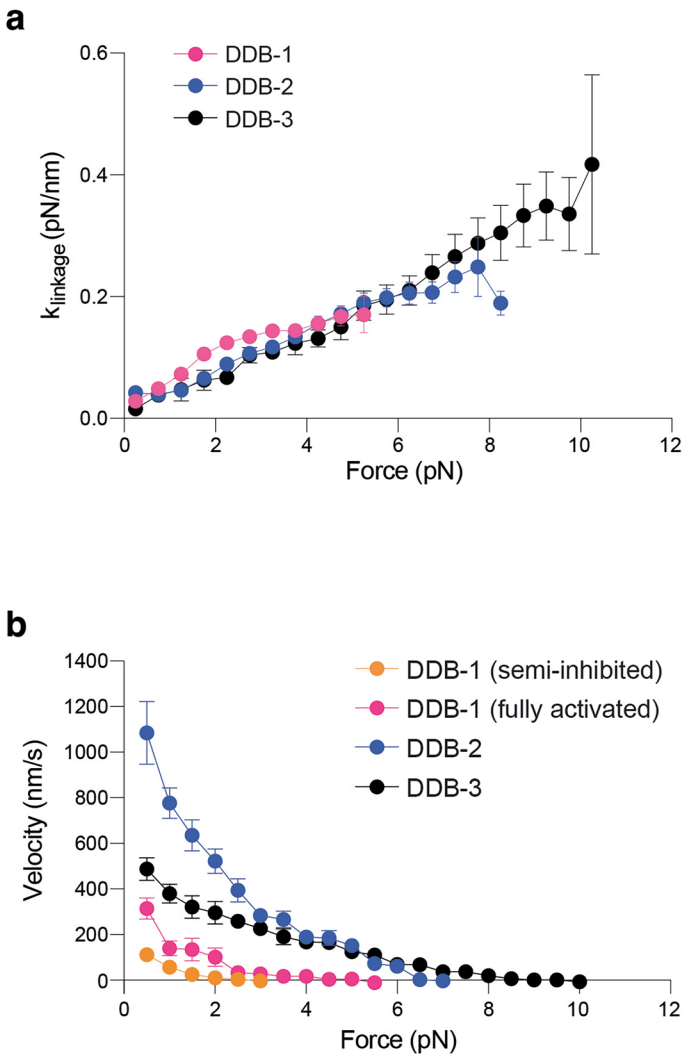

Extended Data Fig. 5 | Force-dependent stiffness and velocity of DDB complexes. a, Measured stiffness ($k_{linkage}$) of DDB complexes as a function of applied force. Bars indicate mean values; error bars represent SEM. Red, D_1DB; blue, D_2DB; black, D_3DB. **b**, Velocity of DDB complexes as a function of applied force. Force-time traces were segmented into ±0.5 pN windows (starting at 0.5 pN and increasing in 0.5-pN steps), and velocity in each window was obtained by linear fitting. This analysis was repeated across multiple stalling traces ($n = 3–40$) to calculate the mean velocity and SEM for each force. Error bars represent SEM; when not visible, they are smaller than the symbol. Colour key: Orange, DDB-1 (semi-inhibited); Pink, D_1DB (fully activated); Blue, D_2DB; Black, D_3DB.

https://doi.org/10.1038/s41556-026-01877-0

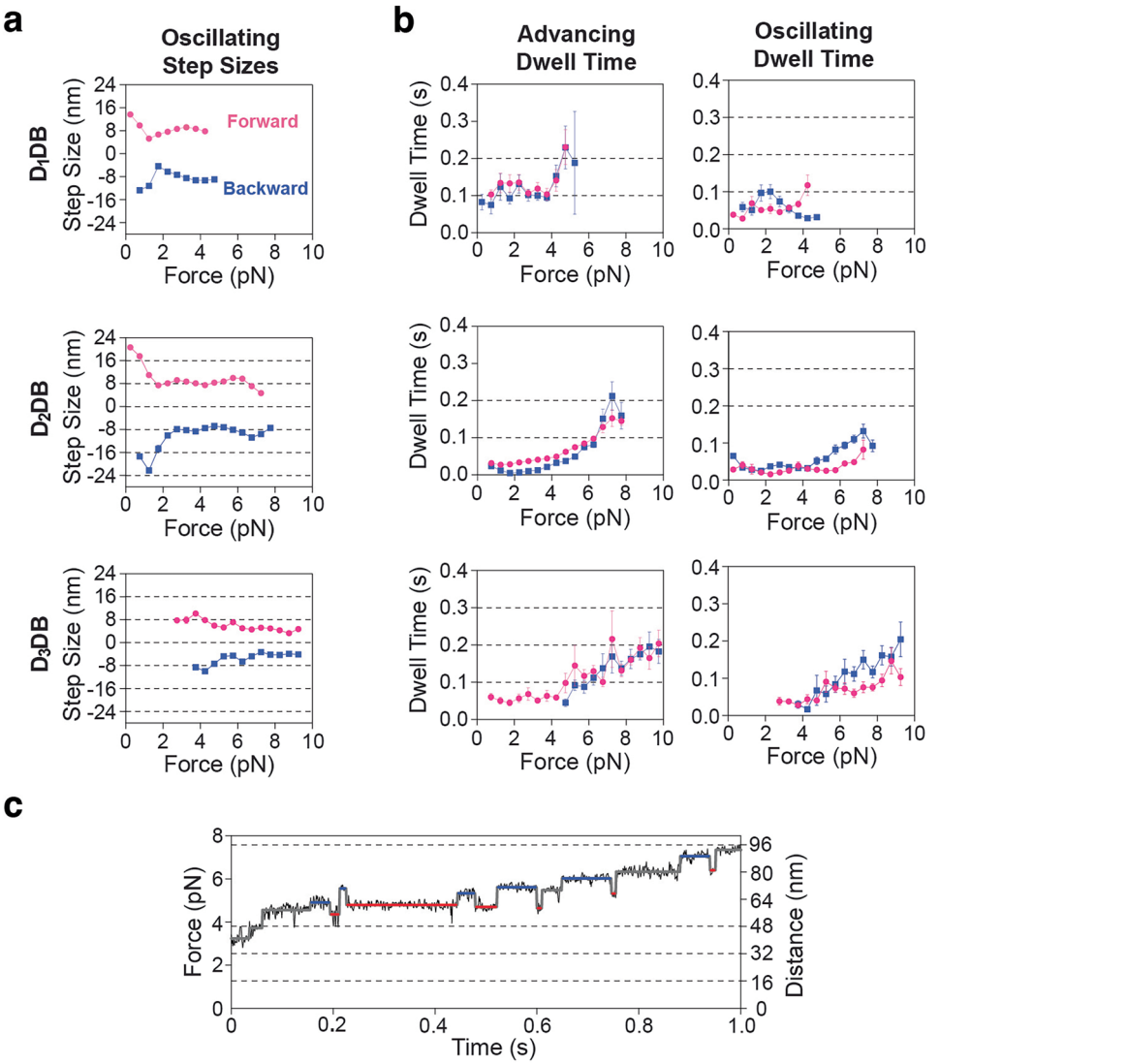

Extended Data Fig. 6 | Step sizes and dwell times for DDB complexes during oscillatory forward–backward stepping. a, Forward and backward step sizes as a function of force of DDB during the oscillatory forward-stepping stepping. Points represent mean ± s.e.m. (error bars are smaller than the symbols and not visible). **b**, Dwell times as a function of force of DDB complexes for both the advancing and oscillatory stepping modes. **c**, Example trace showing segments of forward–backward steps of D_2DB.

nature portfolio

Corresponding author(s): Lu Rao and Arne Gennerich

Last updated by author(s): Oct 31, 2025

Reporting Summary

Nature Portfolio wishes to improve the reproducibility of the work that we publish. This form provides structure for consistency and transparency in reporting. For further information on Nature Portfolio policies, see our Editorial Policies and the Editorial Policy Checklist.

Statistics

For all statistical analyses, confirm that the following items are present in the figure legend, table legend, main text, or Methods section.

n/a	Confirmed	
☐	☒	The exact sample size (*n*) for each experimental group/condition, given as a discrete number and unit of measurement
☐	☒	A statement on whether measurements were taken from distinct samples or whether the same sample was measured repeatedly
☐	☒	The statistical test(s) used AND whether they are one- or two-sided *Only common tests should be described solely by name; describe more complex techniques in the Methods section.*
☒	☐	A description of all covariates tested
☒	☐	A description of any assumptions or corrections, such as tests of normality and adjustment for multiple comparisons
☐	☒	A full description of the statistical parameters including central tendency (e.g. means) or other basic estimates (e.g. regression coefficient) AND variation (e.g. standard deviation) or associated estimates of uncertainty (e.g. confidence intervals)
☐	☒	For null hypothesis testing, the test statistic (e.g. *F*, *t*, *r*) with confidence intervals, effect sizes, degrees of freedom and *P* value noted *Give P values as exact values whenever suitable.*
☒	☐	For Bayesian analysis, information on the choice of priors and Markov chain Monte Carlo settings
☒	☐	For hierarchical and complex designs, identification of the appropriate level for tests and full reporting of outcomes
☒	☐	Estimates of effect sizes (e.g. Cohen's *d*, Pearson's *r*), indicating how they were calculated

Our web collection on statistics for biologists contains articles on many of the points above.

Software and code

Policy information about availability of computer code

Data collection	A Lumicks C-trap/IRM/TIRF with BlueLake software was used for optical tweezers-based data collection. A BioVision four-color TIRF scope with VisView software was used for single-molecule fluorescence-based data collection. A Refeyn mass photometer with AcquireMP software was used for mass photomer-based data collection.
Data analysis	Data were analyzed using a custom-written MATLAB program as previously described in Nicholas et al. 2015 (PNAS). Microsoft Excel Prism-GraphPad ImageJ2 v 2.14.0 Refeyn-DiscoverMP

For manuscripts utilizing custom algorithms or software that are central to the research but not yet described in published literature, software must be made available to editors and reviewers. We strongly encourage code deposition in a community repository (e.g. GitHub). See the Nature Portfolio guidelines for submitting code & software for further information.

Data

Policy information about availability of data

All manuscripts must include a data availability statement. This statement should provide the following information, where applicable:

- Accession codes, unique identifiers, or web links for publicly available datasets
- A description of any restrictions on data availability
- For clinical datasets or third party data, please ensure that the statement adheres to our policy

The datasets generated during and/or analyzed during the current study are available from the corresponding author on reasonable request.

Research involving human participants, their data, or biological material

Policy information about studies with human participants or human data. See also policy information about sex, gender (identity/presentation), and sexual orientation and race, ethnicity and racism.

Reporting on sex and gender	N.A.
Reporting on race, ethnicity, or other socially relevant groupings	N.A.
Population characteristics	N.A.
Recruitment	N.A.
Ethics oversight	N.A.

Note that full information on the approval of the study protocol must also be provided in the manuscript.

Field-specific reporting

Please select the one below that is the best fit for your research. If you are not sure, read the appropriate sections before making your selection.

☒ Life sciences ☐ Behavioural & social sciences ☐ Ecological, evolutionary & environmental sciences

For a reference copy of the document with all sections, see nature.com/documents/nr-reporting-summary-flat.pdf

Life sciences study design

All studies must disclose on these points even when the disclosure is negative.

Sample size	Sample sizes were determined to be able to draw statistically meaningful conclusion as previously described in Nicholas et al. 2015 (PNAS).
Data exclusions	No data were excluded from the analyses.
Replication	Single-molecule motility experiments were done in triplicate (three independent experiments per protein prep).
Randomization	N.A.
Blinding	N.A.

Reporting for specific materials, systems and methods

We require information from authors about some types of materials, experimental systems and methods used in many studies. Here, indicate whether each material, system or method listed is relevant to your study. If you are not sure if a list item applies to your research, read the appropriate section before selecting a response.

Materials & experimental systems

n/a	Involved in the study
☐	☒ Antibodies
☐	☒ Eukaryotic cell lines
☒	☐ Palaeontology and archaeology
☒	☐ Animals and other organisms
☒	☐ Clinical data
☒	☐ Dual use research of concern
☒	☐ Plants

Methods

n/a	Involved in the study
☒	☐ ChIP-seq
☒	☐ Flow cytometry
☒	☐ MRI-based neuroimaging

Antibodies

Antibodies used: Anti-GFP antibodies were purified from rabbit serum as previously described by Nicholas et al. 2015 (PNAS).

Validation: Antibodies were purified using an affinity column bearing purified GFP with a GST (glutathione S-transferase) tag (GSTGFP) and the GFP-tagged constructs used in this study only bound to trapping beads when coated with the purified anti-GFP antibody.

Eukaryotic cell lines

Policy information about cell lines and Sex and Gender in Research

Cell line source(s): HEK-293.2sus was purchased from ATCC.

Authentication: Cell lines were not authenticated.

Mycoplasma contamination: Cell lines were not tested for mycoplasma contamination.

Commonly misidentified lines (See ICLAC register): No commonly misidentified lines per ICLAC register were used.

Plants

Seed stocks: *Report on the source of all seed stocks or other plant material used. If applicable, state the seed stock centre and catalogue number. If plant specimens were collected from the field, describe the collection location, date and sampling procedures.*

Novel plant genotypes: *Describe the methods by which all novel plant genotypes were produced. This includes those generated by transgenic approaches, gene editing, chemical/radiation-based mutagenesis and hybridization. For transgenic lines, describe the transformation method, the number of independent lines analyzed and the generation upon which experiments were performed. For gene-edited lines, describe the editor used, the endogenous sequence targeted for editing, the targeting guide RNA sequence (if applicable) and how the editor was applied.*

Authentication: All protein constructs were validated via DNA sequencing, and all reagents used were obtained from reputable commercial suppliers, as detailed in the materials and methods section.